The Astrophysical Journal Supplement Series, 264:9 (18pp), 2023 January https://doi.org/10.3847/1538-4365/ac9ea8

A Southern Photometric Quasar Catalog from the Dark Energy Survey Data Release 2

Qian Yang[1,2] and Yue Shen[1,2]
[1] Department of Astronomy, University of Illinois at Urbana-Champaign, Urbana, IL 61801, USA; qian.yang@cfa.harvard.edu
[2] National Center for Supercomputing Applications, University of Illinois at Urbana-Champaign, Urbana, IL 61801, USA
Received 2022 June 17; revised 2022 October 4; accepted 2022 October 6; published 2022 December 16

Abstract

We present a catalog of 1.4 million photometrically selected quasar candidates in the southern hemisphere over the ∼5000 deg^2 Dark Energy Survey (DES) wide survey area. We combine optical photometry from the DES second data release (DR2) with available near-infrared (NIR) and the all-sky unWISE mid-infrared photometry in the selection. We build models of quasars, galaxies, and stars with multivariate skew-*t* distributions in the multidimensional space of relative fluxes as functions of redshift (or color for stars) and magnitude. Our selection algorithm assigns probabilities for quasars, galaxies, and stars and simultaneously calculates photometric redshifts (photo-*z*) for quasar and galaxy candidates. Benchmarking on spectroscopically confirmed objects, we successfully classify (with photometry) 94.7% of quasars, 99.3% of galaxies, and 96.3% of stars when all IR bands (NIR *YJHK* and WISE W1W2) are available. The classification and photo-*z* regression success rates decrease when fewer bands are available. Our quasar (galaxy) photo-*z* quality, defined as the fraction of objects with the difference between the photo-*z* z_p and the spectroscopic redshift z_s, $|\Delta z| \equiv |z_s - z_p|/(1+z_s) \leqslant 0.1$, is 92.2% (98.1%) when all IR bands are available, decreasing to 72.2% (90.0%) using optical DES data only. Our photometric quasar catalog achieves an estimated completeness of 89% and purity of 79% at $r < 21.5$ (0.68 million quasar candidates), with reduced completeness and purity at $21.5 < r \lesssim 24$. Among the 1.4 million quasar candidates, 87,857 have existing spectra, and 84,978 (96.7%) of them are spectroscopically confirmed quasars. Finally, we provide quasar, galaxy, and star probabilities for all (0.69 billion) photometric sources in the DES DR2 coadded photometric catalog.

Unified Astronomy Thesaurus concepts: Quasars (1319); Sky surveys (1464); Catalogs (205); Redshift surveys (1378)

1. Introduction

Active galactic nuclei (AGNs) and their high-luminosity counterparts, quasars, are accreting supermassive black holes (SMBHs) at the center of massive galaxies. Understanding the evolution of the quasar population across cosmic time is crucial to understanding the physics of accretion and the coevolution of SMBHs and their host galaxies.

Large quasar surveys provide the necessary samples for measuring the abundance of quasars as functions of redshift and luminosity. In addition, these surveys enable a broad range of quasar science, such as quasar lens searches and their constraints on cosmology and the evolution of massive galaxies (e.g., Oguri et al. 2006, 2012), finding projected quasar pairs (e.g., Hennawi et al. 2006a; Prochaska et al. 2013) and binary quasars (e.g., Hennawi et al. 2006b, 2010), and measuring quasar clustering (e.g., Martini & Weinberg 2001; Shen et al. 2007). Large quasar surveys also provide an opportunity to identify rare objects, such as extreme variability quasars (e.g., Rumbaugh et al. 2018), and study their fueling mechanisms (e.g., MacLeod et al. 2016; Yang et al. 2018). Finally, large samples of quasars are often used to define the celestial reference frame (e.g., Gaia Collaboration et al. 2018a).

Distant quasars have been discovered beyond redshift 7 (Mortlock et al. 2011; Bañados et al. 2018; Yang et al. 2020; Wang et al. 2021), where massive SMBHs formed within less than 1 billion yr after the Big Bang. A large sample of quasars over a broad range of redshifts enables the study of the evolution of SMBHs, as well as the intergalactic medium. For example, the Lyα forest in quasar spectra can be used to measure baryon acoustic oscillations as a probe for cosmology (Dawson et al. 2013).

While the Sloan Digital Sky Survey (SDSS; York et al. 2000) has provided large samples of quasars in the northern hemisphere, there is a lack of large spectroscopically confirmed quasar samples in the southern hemisphere. There are over 750,000 quasars in the SDSS DR16 quasar catalog (Lyke et al. 2020). In contrast, there are less than 24,000 spectroscopically confirmed quasars in the southern hemisphere in the Million Quasars Catalog (v6.5; Flesch 2019) with decl. $< -10°$. A large sample of quasars in the southern hemisphere will be important for quasar-related studies in the next few decades, given increasing investments of ground-based facilities covering the southern sky, in particular, the Vera C. Rubin Observatory Legacy Survey of Space and Time (Ivezić et al. 2019).

The Dark Energy Survey (DES; Abbott et al. 2018) is a wide-area visible and near-infrared (NIR) imaging survey covering ∼5000 deg^2 of the high-Galactic-latitude sky, mostly in the southern hemisphere. The multiband deep DES photometry enables the photometric selection of a large quasar sample in the southern hemisphere. In this work, we perform a systematic selection of quasar candidates using public photometric data from DES over the ∼5000 deg^2 wide survey footprint, combined with publicly available NIR and mid-infrared (MIR) photometric data. With these data, we classify quasars, galaxies, and stars in all DES-detected photometric sources with probabilities and estimated photo-*z*s (for galaxy and quasar candidates).

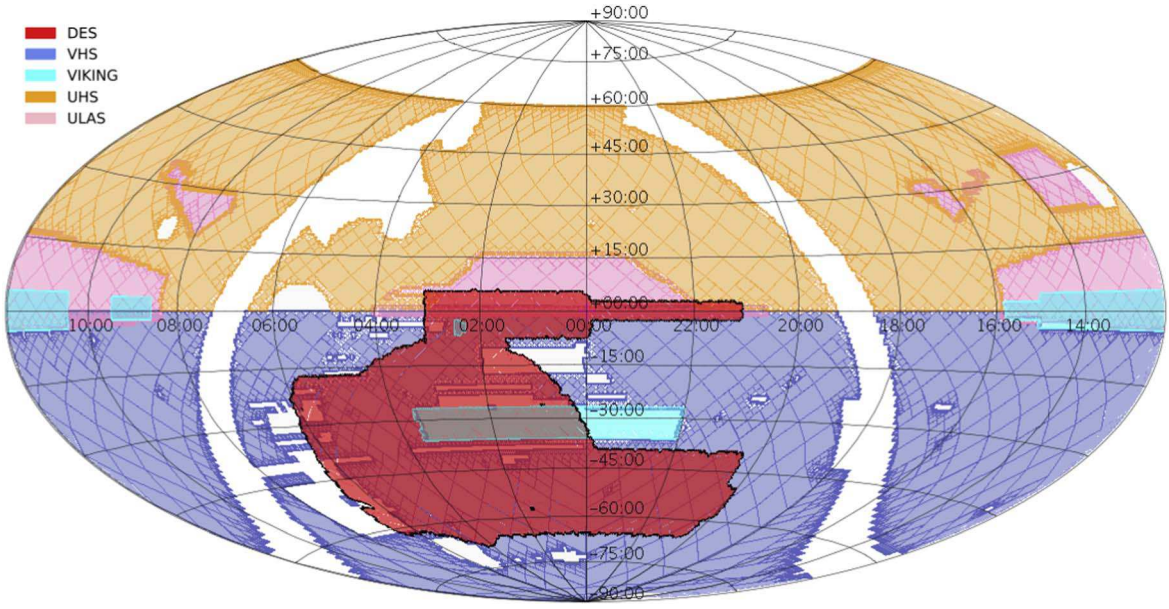

Figure 1. Sky coverage of the DES and NIR surveys in equatorial coordinates. WISE, 2MASS, and Gaia are all-sky surveys and not shown here. DES: shaded red area with black outline; VHS: shaded blue area with meshes; VIKING: shaded cyan area; UHS: shaded orange area with meshes; ULAS: shaded pink area with meshes. These NIR surveys (except for 2MASS) barely overlap with each other. For areas not covered by VHS, VIKING, UHS, or ULAS, we used 2MASS NIR data.

Table 1
Photometric Survey

Survey	Data Release	Area (deg^2)	Filter	Depth (AB, 5σ)
DES	DR2	5000	g, r, i, z, Y	25.0, 24.5, 23.7, 22.6, 21.3
VIKING	DR5	1500	Y, J, H, K_s	21.9, 21.8, 21.2, 21.1
VHS	DR6	8300	Y, J, H, K_s	20.7, 21.0, 20.5, 20.2
ULAS	DR11	4000	Y, J, H, K	21.0, 20.7, 20.3, 20.2
UHS	DR1	12,700	J	20.3
2MASS	···	All sky	J, H, K_s	18.0, 17.6, 17.4
unWISE	NEO6	All sky	W1, W2	21.7, 20.9
Gaia	DR2	All sky	···	···

Note. NEO6: up to year 6 of NEOWISE-Reactivation. We only use astrometry information from Gaia DR2.

The structure of this paper is as follows. In Section 2, we describe the imaging surveys and training samples. We describe the selection methods in Section 3. We present the quasar catalog in Section 4 and discuss the selection completeness and efficiency in Section 5. We conclude in Section 6. Throughout this paper, we adopt a flat ΛCDM cosmology with parameters $\Omega_\Lambda = 0.7$, $\Omega_m = 0.3$, and $H_0 = 70$ km s^{-1} Mpc^{-1}. The Milky Way extinctions of extragalactic objects in DES bands are corrected using the dust reddening map of Schlegel et al. (1998). In this work, the term "quasar" is used to broadly refer to an unobscured broad-line AGN regardless of its luminosity. We also only consider quasar targets where the continuum emission is dominated by the quasar rather than the host galaxy.

2. Data and Samples

2.1. Imaging Surveys

We use the second public data release (DR2) of the DES (Abbott et al. 2021), including data from the DES wide-area survey covering ∼5000 deg^2 of the southern Galactic cap in five broad photometric bands (*grizY*). We use the DES DR2 coadded photometric catalog, including ∼691 million distinct astronomical objects, the vast majority of which are nontransient and nonmoving objects. For the DES coadded photometry, we use the IMAFLAGS_ISO flag to remove unreliable detections, which is set if any pixel is masked in all of the contributing exposures for a give band. This flag is mainly set for saturated objects and objects with missing data (Abbott et al. 2018). The median coadded catalog point-source depths at S/N = 5 in the *grizY* bands are 25.0, 24.5, 23.7, 22.6, and 21.3, respectively (point-spread function, PSF, mag). We use both PSF and AUTO photometry in DES depending on the fitting template class (see below).

For the NIR data, we make use of all public NIR imaging in the DES area, including the VISTA Hemisphere Survey (VHS; McMahon et al. 2013), the VISTA Kilo-Degree Infrared Galaxy Survey (VIKING; Edge et al. 2013), the UKIDSS Large Area Surveys (ULAS; Lawrence et al. 2007), and the UKIRT Hemisphere Survey (UHS; Dye et al. 2018). For these NIR surveys, we use the aperture-corrected magnitude in a 2″ diameter circle. For areas not covered by these NIR surveys, we use the shallower all-sky Two Micron All Sky Survey (2MASS; Skrutskie et al. 2006) data. Figure 1 shows the sky coverages of different NIR imaging surveys. The VHS survey covers most of the DES area in the southern sky. We summarize the depths of these NIR surveys in Table 1. We ignore the slight filter differences among different NIR surveys,

Table 2
Spectroscopically Confirmed Training Samples

Class	QSO				Galaxy	Star		
Database	All	SDSS	Milliquas	Simulation	All (SDSS)	All	SDSS	LAMOST
Sample size	1,252,844	744,293	63,948	444,603	2,655,705	4,426,020	1,028,777	3,397,243
DES	102,321	85,181	17,140	⋯	318,438	160,165	40,141	120,024
DES (filter)	1,023,645	579,042	⋯	444,603	1,520,671	426,334	426,334	⋯
unWISE	1,239,666	733,102	61,961	444,603	2,614,053	4,277,893	914,133	3,363,760
Gaia	518,584	468,385	50,199	⋯	335,923	4,185,994	819,135	3,366,859
NIR (Y)	631,885	155,399	31,883	444,603	857,511	1,200,916	276,327	924,589
NIR (J)	859,988	367,988	47,397	444,603	2,068,340	4,104,015	731,234	3,372,781
NIR (H)	628,567	148,225	35,739	444,603	1,402,542	3,850,179	506,919	3,343,260
NIR (K)	646,936	163,652	38,681	444,603	1,430,952	3,766,737	469,049	3,297,688

Note. We use spectroscopically confirmed quasars/galaxies/stars from SDSS, quasars in the Million Quasars Catalog (Milliquas), and stars from LAMOST as our training samples. We crossmatch the spectroscopically confirmed samples with source catalogs from various imaging surveys, including DES, unWISE, Gaia, and NIR surveys (described in Section 2.1). Since most SDSS sources are in the northern sky and not covered by DES, we convolve the SDSS spectra with the DES filter curves to generate synthetic DES photometry. To improve the color coverage of high-redshift quasars, we add simulated high-redshift quasars (see Section 2.2).

which result in minor magnitude differences (normally less than 0.05 mag).

In the MIR, we use the unblurred coadds of the Wide-field Infrared Survey Explorer (WISE; Wright et al. 2010) imaging data (unWISE; Lang 2014; Meisner et al. 2019). We use the unWISE photometry from coadds of WISE and NEOWISE (through the sixth year NEOWISE data release in 2020). The unWISE catalog has advantages over the AllWISE catalog (Wright et al. 2019), since it is based on significantly deeper imaging and features improved photometric modeling in crowded regions (Schlafly et al. 2019). The 5σ depth in AB magnitude in the unWISE W1 and W2 bands is 21.7 and 20.9, respectively.

Gaia DR2 (Gaia Collaboration et al. 2018b) contains celestial positions for 1.7 billion sources and parallaxes and proper motions for 1.3 billion sources. We use Gaia astrometry information to help rule out stars with detected proper motion or parallax.

2.2. Training Samples

We consider three object classes, quasars, stars, and galaxies, for which we build empirical color templates from training samples. Stars and most quasars are pointlike objects, and galaxies are mostly extended sources. Each object is fit to three classes of color templates (quasar, star, and galaxy). When fitting with quasar and star templates, we default to use DES PSF photometry for the object. When fitting with the galaxy template, we default to use the AUTO photometry in DES. At the faint end, for some objects without DES PSF photometry in some bands, we use the DES AUTO photometry for all three classes.

We then use spectroscopically confirmed quasars, stars, and galaxies to build our color templates. For quasars, we start from the SDSS DR16 quasar catalog (Lyke et al. 2020) but remove unreliable high-redshift quasars misclassified by the SDSS pipeline. Specifically, we removed $z > 5$ quasars that were only classified as "QSO" by the pipeline but not confirmed by visual inspection (most of these are pipeline misclassifications of low-redshift quasars or nonquasars). Next, we supplement spectroscopically confirmed quasars from the Million Quasars Catalog v6.5 (Flesch 2019). We added sources with types "Q" and "A," which are broad-line quasars and broad-line Seyferts, respectively. This supplementary sample is necessary because it includes confirmed high-redshift quasars at $z > 5$ and quasars from the 2dF QSO Redshift Survey (Croom et al. 2004), the 2dF-SDSS LRG and QSO survey (Croom et al. 2009), the Australian Dark Energy Survey (Yuan et al. 2015), and the Large Sky Area Multi-object Fiber Spectroscopic Telescope (LAMOST) quasar catalog (Yao et al. 2019). The redshifts of the majority of the spectroscopically confirmed quasars are lower than 3.5 (99% of SDSS quasars). The number of spectroscopically confirmed quasars decreases rapidly with redshift, specifically from 9178 at $3 < z < 3.1$, to 634 at $4 < z < 4.1$, to 37 at $6 < z < 6.1$. So, at the high-redshift end, using only these confirmed quasars may lead to strong biases from individual quasars. To improve the color coverage of $z > 3.5$ quasars, we add simulated quasars (McGreer et al. 2013) at high redshift ($z = 3.5$–8).[3] The simulated quasar models include a broken power-law continuum, UV/optical emission lines, pseudocontinuum from Fe II emission, and redshift-dependent Lyα forest absorption due to neutral hydrogen. The numbers per redshift bin of simulated $z > 3.5$ quasars are close to those of SDSS quasars at $1.5 < z < 3.5$. We simulated a large number of quasars to ensure a sufficient statistical sample to avoid the impact of random fluctuations.

We consider contamination from stars and galaxies in our quasar selection. We use spectroscopic galaxies and stars from the SDSS DR16 (Ahumada et al. 2020). The SDSS galaxies are representative of the low-redshift galaxy population but limited to $z \lesssim 1$ given the nature of optical SDSS surveys. However, the lack of representation of $z \gtrsim 1$ galaxies in the training sample does not affect our quasar selection, since these high-z galaxies are typically much fainter in the observed-frame optical than our quasar targets. We supplement the sample with stars from the fifth data release of the LAMOST survey (Luo et al. 2015). We restrict this to high-Galactic-latitude stars in LAMOST with $|b| > 20°$, as the DES footprint is all at $|b| > 20°$. Compared with SDSS, the supplemental LAMOST stars are mainly at the bright end ($i < 18$). The star training sample is representative of different types of stars, from white dwarfs to late-type stars. For example, more than half of the 68,000 white dwarfs from the Montreal White Dwarf Database[4] are in our star training sample, and the other half are mainly out

[3] The DECam Y band extends to ~10700 Å. Therefore, at $z > 7.8$, the Lyα emission of quasars starts to drop out of the DES Y band.
[4] http://www.montrealwhitedwarfdatabase.org

of the SDSS sky coverage. Among the 10,000 brown dwarfs compiled by Best et al. (2018) from the DwarfArchives,[5] 83% of them are in our star training sample.

We summarize the number of different classes of objects from different catalogs in Table 2. We cross-matched the sources with the imaging surveys described in Section 2.1 with a search radius of 2″. The number of sources detected by different imaging surveys is also included in Table 2. Since most SDSS sources are in the northern sky and not covered by DES, we convolve the SDSS spectra with the DES filter curves to generate synthetic DES photometry in the training samples. Because the DES Y band spans from ∼9400 to ∼10700 Å, we do not use spectra taken by the SDSS-I/II spectrographs (only up to 9200 Å) and instead use spectra taken by the SDSS BOSS spectrographs (up to 10400 Å) whenever applicable.

3. Target Selection Algorithms

3.1. General Considerations

The photo-z problem is a regression problem, relying on the description of the probability distribution of redshift for a specific class of objects. Quasar target selection is a classification problem, depending on the probability estimates for different classes of objects, such as quasars, stars, and galaxies.

We briefly describe the prior, likelihood, and posterior probabilities in our Bayesian analysis. In Bayes' theorem, the posterior probability of the model parameters θ given data x can be written as

$$p(\theta|\boldsymbol{x}) = \frac{p(\boldsymbol{x}|\theta)p(\theta)}{p(\boldsymbol{x})} \propto \mathcal{L}(\theta)p(\theta), \quad (1)$$

where $\mathcal{L}(\theta) = p(\boldsymbol{x}|\theta)$ is the likelihood, and $p(\theta)$ is the prior probability of model parameters θ. Here $p(\boldsymbol{x})$ is the normalizing constant (also called evidence) and is usually ignored in the inference.

In our photo-z regression problem, θ is the redshift, and $\boldsymbol{x}$ is the multidimensional relative flux (i.e., flux ratio with regard to the flux in a reference band). The prior distribution, $N(z)$, is the predicted number distribution of an object class (i.e., quasar or galaxy) as a function of redshift z. We describe the prior distribution in Section 3.2 and likelihood distribution in Section 3.3.

3.2. Prior Distribution

The number densities of quasars and galaxies depend on redshift and luminosity, which can be estimated using the observed luminosity functions of quasars and galaxies. The number density of stars depends on stellar type and luminosity, as well as locations in the sky. All of these number densities refer to the absolute sky densities of the three classes of objects.

We implement the optical quasar luminosity function (QLF) from Palanque-Delabrouille et al. (2016), which is based on quasars over a wide redshift range of $0.68 < z < 4.0$ and magnitudes as faint as 22.5 mag in the g band. We extrapolate this QLF to the faint end and the high-redshift end. We also tested the bolometric QLFs from Hopkins et al. (2007) and Shen et al. (2020). However, there are additional issues of utilizing these bolometric QLFs due to uncertainties in bolometric corrections and k-corrections, which are redshift- and luminosity-dependent. The QLF from Palanque-Delabrouille et al. (2016) works well for quasar photo-z estimation over broad ranges of redshift and optical magnitude (Yang et al. 2017), as desired here.

We implement the galaxy luminosity function (GLF) from Montero-Dorta & Prada (2009) based on SDSS data. There are different subclasses of galaxies, such as late- and early-type galaxies. Our galaxy training sample is not rigorously labeled with different subtypes, lacking information such as star formation rate or morphology. So we simply treat all galaxies as a single class in this work. Most of these SDSS galaxies are at $z < 1$, with a small fraction of them at higher redshifts. Since there are very few spectroscopically confirmed galaxies at $z \geqslant 1.5$ (<0.02%) in the training sample, we restrict to $z < 1.5$. Galaxies at $z > 1.5$ are too faint in the observed-frame optical to contaminate our quasar selection.

We estimate the number density of stars for typical high-Galactic-latitude fields[6] from a Milky Way synthetic simulation with the Besançon model (Robin et al. 2003). Yang et al. (2017) showed that the simulated star number distribution is close to the observed distribution. We performed such a simulation of stars with DES filters in a 100 deg^2 region with a central position at R.A. = 2 hr and decl. = −36°, which is close to the median central position of the DES survey. The number density of stars also depends on stellar types. Our star training sample is not well labeled into different stellar types. Instead, we use color, c, as an alternative parameter for different stellar types. We describe what colors are used specifically for stars in Section 3.3.

Using the QLF, GLF, and star simulations described above, we derive the quasar number (per deg^2) prior distribution as a function of redshift, $N_{\rm QSO}(z)$; the galaxy number prior distribution as a function of redshift, $N_{\rm Galaxy}(z)$; and the star number prior distribution as a function of color, $N_{\rm Star}(c)$, in a set of magnitude bins. Our algorithm can be improved with a better QLF and GLF for a wider range of redshifts and magnitudes. Our galaxy photo-z can be further improved with galaxy training samples and GLFs labeled with different subtypes.

3.3. Likelihood Function

The key problem of our target selection/classification is to describe the likelihood of a series of attributes, $\boldsymbol{x}$, for a given redshift and magnitude. Specifically, in our algorithm, $\boldsymbol{x}$ represents the multidimensional relative fluxes.

The colors of quasars change as a function of redshift due to the shift of quasar emission lines moving in and out of different filters. Quasar colors also change as a function of magnitude for multiple reasons: (1) the colors of the quasar at the faint end or low redshift are more affected by their host galaxy light, (2) quasars are usually bluer when brighter, and (3) the equivalent widths of quasar emission lines are often anticorrelated with the continuum emission (i.e., the Baldwin effect; Baldwin 1997).

The colors of quasars at similar redshifts and magnitudes are usually similar. To fit the color distribution in multidimensional space, we can, for example, (1) fit the color in each color dimension with a Gaussian distribution, such as using the χ^2 method (e.g., Richards et al. 2001); (2) fit the colors in

[5] http://DwarfArchives.org

[6] In principle, our algorithm can implement a stellar number density as a function of Galactic latitude to improve the quasar selection in regions with higher stellar densities. For simplicity, in this work, we only consider the typical stellar density at high Galactic latitudes and leave this additional implementation to future work.

multidimensional space with a multivariate Gaussian distribution, such as using the multivariate χ^2 method (e.g., Weinstein et al. 2004); (3) fit the colors in multidimensional space with a mixture of multiple multivariate Gaussian distributions, such as the XDQSOz technique (Bovy et al. 2011, 2012); (4) fit the colors in multidimensional space with machine-learning techniques (e.g., Yèche et al. 2010; Shu et al. 2019); or (5) fit the colors in multidimensional space with more flexible parametric distribution, such as the multivariate skew-*t* distribution (Yang et al. 2017).

Skewt-QSO is an algorithm for quasar selection and photo-*z* estimation (Yang et al. 2017). The color distribution of quasars shows skewed and tail features mainly due to intrinsic dust reddening. Skewt-QSO describes the color distribution of quasars in a specific redshift and magnitude range by multivariate skew-*t* distributions. Yang et al. (2017) demonstrated that the skew-*t* distribution better describes the color distribution of quasars than Gaussian or skew-normal distributions. Skewt-QSO also achieves better photo-*z* accuracy compared to other quasar photo-*z* algorithms, such as the empirical color–redshift relation (e.g., Richards et al. 2001; Weinstein et al. 2004) and the XDQSOz algorithm (Bovy et al. 2012). Here we briefly describe the skewt-QSO algorithm (see more details in Yang et al. 2017).

The probability density function (PDF) of a multivariate skew-*t* distribution, denoted by $ST_n(\boldsymbol{\mu}, \boldsymbol{\Sigma}, \boldsymbol{\lambda}, \nu)$, can be expressed as (Lachos et al. 2014)

$$2\, t_n(\boldsymbol{x}|\boldsymbol{\mu}, \boldsymbol{\Sigma}, \nu)\, T\left(\frac{\sqrt{\nu+n}\ \boldsymbol{\lambda}^{\top}\boldsymbol{\Sigma}^{-1/2}(\boldsymbol{x}-\boldsymbol{\mu})}{\sqrt{\nu+d}}|0,\ 1,\ \nu+n\right), \tag{2}$$

where $\boldsymbol{x}$ is the n-dimensional variate (relative fluxes), $\boldsymbol{\mu}$ is the mean vector, $\boldsymbol{\Sigma}$ is the covariance matrix, ν is the degree of freedom, $\boldsymbol{\lambda}$ is the shape parameter, and d is the Mahalanobis distance $d=(\boldsymbol{x}-\boldsymbol{\mu})^{\top}\boldsymbol{\Sigma}^{-1}(\boldsymbol{x}-\boldsymbol{\mu})$. Here t_n and T denote the PDF and cumulative distribution function (CDF) of the Student-*t* distribution,

$$\frac{\Gamma(\frac{n+\nu}{2})}{\Gamma(\frac{\nu}{2})(\nu\pi)^{n/2}}|\boldsymbol{\Sigma}|^{-1/2}\left(1+\frac{d}{\nu}\right)^{-(\frac{n+\nu}{2})}, \tag{3}$$

where Γ is the gamma function. When $\boldsymbol{\lambda}=0$ and $\nu=\infty$, the skew-*t* distribution becomes the normal distribution, $N_n(\boldsymbol{\mu}, \boldsymbol{\Sigma})$.

As redshift increases, the Lyα emission begins to drop out, and the Lyα forest begins to move into blue bands. We use the relative fluxes instead of colors because at the faint end, even negative flux (e.g., nondetection) is useful. Yang et al. (2017) used the *r* band as the reference band. However, the Lyα emission of $z>5$ quasars begins to drop out of the *r* band. Using a fixed reference band for relative fluxes will lead to large uncertainties for high-redshift quasars. Here we use a flexible reference band to compute relative fluxes. We choose the reference band as the band with the maximum signal-to-noise ratio (S/N) in DES *grizY* photometry.

The likelihood function of the multivariate attribute, $\boldsymbol{x}$, for a given θ can be described by the multivariate skew-*t* distribution. Here $\boldsymbol{x}$ is the multidimensional relative fluxes. For quasars and galaxies, θ is the redshift, z; for stars, θ is the color, c.

To model the colors of quasars (construct the likelihood functions), we divide the quasar training sample described in Section 2.2 into redshift bins of $\Delta z=0.05$ and magnitude bins of $\Delta m=0.1$. This bin size is large enough to enclose enough quasars in one bin and small enough for quasar photo-*z* estimation (Yang et al. 2017). To model the colors of galaxies, we divide the galaxy training sample in redshift bins of $\Delta z=0.01$ and magnitude bins of $\Delta m=0.1$. We divide the star training sample into color bins, where the color (with regard to the reference band) can be treated as a parameter similar to redshift for quasars/galaxies. We use different colors (specifically, $g-r$, $r-i$, $r-i$, $i-z$, or $z-Y$) when the reference band is different (g, r, i, z, or Y). We divide the star training sample into color bins of $\Delta c=0.02$ and magnitude bins of $\Delta m=0.1$. Thus, we obtain a series of skew-*t* parameters ($\boldsymbol{\mu}$, $\boldsymbol{\Sigma}$, $\boldsymbol{\lambda}$, ν) as a function of redshift (or color) and magnitude for quasars, galaxies, and stars, respectively. Using the multivariate skew-*t* distributions with these parameters, we obtain the likelihood functions to describe quasars, galaxies, and stars in the multidimensional color space as a function of redshift (or color) in different magnitude bins.

For an object at a given magnitude with the multivariate attribute $\boldsymbol{x}$ (multidimensional relative fluxes) and their uncertainties, we use Equation (2) to estimate the likelihood in each quasar redshift bin, $\mathcal{L}_{\rm QSO}(z)$; galaxy redshift bin, $\mathcal{L}_{\rm Galaxy}(z)$; and star color bin, $\mathcal{L}_{\rm Star}(c)$.

3.4. Joint Posterior Probability

For an object with available photometric data in multiple bands (so we know its magnitude and multidimensional relative fluxes), we obtain the joint posterior probability (Equation (1)) by combining the prior probability described in Section 3.2 and the likelihood function described in Section 3.3 for quasar, galaxy, and star classes, respectively.

For the quasar class, we obtain the joint posterior probability at each redshift. The quasar class PDF is obtained as

$$p_{\rm QSO}(z) = \mathcal{L}_{\rm QSO}(z) N_{\rm QSO}(z). \tag{4}$$

We identify peaks in the PDF automatically using the *findpeaks* function in the *R pracma* package (Borchers 2022).[7] We obtain the quasar photo-*z*, denoted as photoz-QSO, from the primary peak with the highest integrated probability within a redshift range ($z1$, $z2$), where $z1$ and $z2$ denote the locations of zero probability on both sides of the peak as identified by *pracma*. A parameter $P_{\rm QSOz}$ describing the probability that the true redshift is located within the primary peak, ($z1_{\rm QSO}$, $z2_{\rm QSO}$), can be computed as

$$P_{\rm QSOz} = \frac{\int_{z1_{\rm QSO}}^{z2_{\rm QSO}} p_{\rm QSO}(z)dz}{\int p_{\rm QSO}(z)dz}, \tag{5}$$

which is used to quantify the uncertainty of photoz-QSO.

Similar to the quasar class, the PDF of the galaxy class is

$$p_{\rm Galaxy}(z) = \mathcal{L}_{\rm Galaxy}(z) N_{\rm Galaxy}(z). \tag{6}$$

The identified photo-*z* of the galaxies is denoted as photoz-Galaxy, and the probability that the true redshift is located

[7] https://cran.r-project.org/web/packages/pracma/index.html

within ($z1_{\rm galaxy}$, $z2_{\rm galaxy}$) is

$$P_{\rm Galaxyz} = \frac{\int_{z1_{\rm Galaxy}}^{z2_{\rm Galaxy}} p_{\rm Galaxy}(z)dz}{\int p_{\rm Galaxy}(z)dz}. \quad (7)$$

The PDF of the stars is

$$p_{\rm Star}(c) = \mathcal{L}_{\rm Star}(c)N_{\rm Star}(c). \quad (8)$$

The total probabilities of the quasar, galaxy, and star are

$$\begin{aligned} rclp_{\rm QSO} &= \int p_{\rm QSO}(z)dz, \\ p_{\rm Galaxy} &= \int p_{\rm Galaxy}(z)dz, \\ p_{\rm Star} &= \int p_{\rm Star}(c)dc. \end{aligned} \quad (9)$$

Therefore, the normalized probability of an object being a quasar is expressed as

$$P_{\rm QSO} = \frac{p_{\rm QSO}}{p_{\rm QSO} + p_{\rm Star} + p_{\rm Galaxy}}. \quad (10)$$

The quasar candidate selection flowchart is shown in Figure 2. For a given object with relative fluxes and magnitudes, we calculate the posterior probability of the object being a quasar, galaxy, or star combining their likelihood and prior probabilities. We compare these probabilities and classify the candidate as a quasar, galaxy, or star when $P_{\rm QSO}$, $P_{\rm Galaxy}$, or $P_{\rm Star}$ is the maximum probability, respectively. By construction, these three probabilities are normalized to have a unity sum, i.e., $P_{\rm QSO} + P_{\rm Galaxy} + P_{\rm Star} = 1$. We also obtain photoz-QSO for quasar candidates and photoz-Galaxy for galaxy candidates.

3.5. Proper Motions and Parallaxes

It has been shown that proper-motion and parallax detections from Gaia can help reduce stellar contamination in photometric quasar selection (e.g., Calderone et al. 2019; Shu et al. 2019; Wolf et al. 2020). We define the parallax significance, PLXSIG, as

$$\left| \frac{\rm parallax}{\rm parallax\_error} \right|, \quad (11)$$

where parallax_error is the measurement uncertainty of the parallax.

Following Hambly et al. (2008), we define the proper-motion significance, PMSIG, as

$$\frac{\rm pmra^2 + pmdec^2}{\sqrt{(\rm pmra^2\ pmra\_error^2 + pmdec^2\ pmdec\_error^2)}}, \quad (12)$$

where pmra (pmra_error) is the proper motion (measurement error) in R.A., and pmdec (pmdec_error) is the proper motion (measurement error) in decl.[8] We use PLXSIG < 5 and PMSIG < 5 as additional criteria in our quasar target selection to exclude stars.

[8] This PMSIG definition neglects correlated errors in pmra and pmdec.

4. Results

4.1. Photo-z Regression and Classification Results

Table 3 summarizes the photo-z regression and classification results for spectroscopically confirmed objects (quasars, galaxies, and stars) for different photometric band combinations. In total, we used the 15 most frequent photometric band combinations. In general, the photo-z regression and classification results are better when more bands are used, as expected.

The difference between the photo-z (z_p) and the spectroscopic redshift (z_s) is quantified as $|\Delta z| \equiv |z_s - z_p|/(1 + z_s)$. The photo-$z$ accuracy $R_{0.1}$ is the fraction of objects in a test sample with $|\Delta z|$ smaller than 0.1. A larger $R_{0.1}$ represents a higher photo-z accuracy. In addition, a smaller standard deviation of Δz measured for the test sample, $\sigma(\Delta z)$, would indicate that the photo-z result is better overall. When using the *grizY* bands from DES combined with all available IR bands (*YJHK* in NIR and W1W2 in MIR), the photo-z accuracy is as good as 92.2% for quasars and 98.1% for galaxies for our spectroscopic training samples. The standard deviation of Δz, $\sigma(\Delta z)$, is 0.147 and 0.035 for quasars and galaxies, respectively.

As shown in Table 3, with fewer bands, $R_{0.1}$ decreases and $\sigma(\Delta z)$ increases for both quasars and galaxies, as expected. When only using DES bands, $R_{0.1} = 72.2\%$ for quasars and 90.0% for galaxies; $\sigma(\Delta z) = 0.273$ and 0.085 for quasars and galaxies, respectively. For comparison, $R_{0.1} = 74.2\%$ and $\sigma(\Delta z) = 0.27$ for quasars when only using SDSS *ugriz* bands (Yang et al. 2017). The photoz-QSO accuracy using DES photometry is slightly worse than that using SDSS photometry because there is no *u* band in DES, which is useful for quasar photo-z calculation at low redshift. As shown in Yang et al. (2017), $R_{0.1}$ is 72.8% and $\sigma(\Delta z)$ is 0.31 using the XDQSOz method (Bovy et al. 2012). Using our algorithm and the DES photometric data, the photo-z accuracy is comparable to or slightly better than the XDQSOz algorithm using SDSS photometry.

Figure 3 shows the photo-z versus the spectroscopic redshift with the fewest bands (DES only; top panels) and most bands (DES_YJHK_W1W2; bottom panels) for quasars (left panels) and galaxies (right panels). The color map shows the number density. For quasars, using DES data alone, there is an apparent degeneracy between $z \sim 2.2$ and 0.8, since the DES colors of quasars at both redshifts are similar to the C IV (Mg II) line shifts into the *g* band at $z \sim 2.2$ ($z \sim 0.8$). This degeneracy is resolved with the inclusion of NIR and MIR data. For galaxies, there is some degeneracy at $z > 0.5$, and this problem is also alleviated by including NIR and MIR data.

Our algorithm not only calculates quasar and galaxy photo-z but also classifies quasars, galaxies, and stars based on the maximum probability. In Table 3, we show the fraction of objects classified as quasars, galaxies, and stars in the spectroscopic training samples. We used the $P_{\rm QSO}$, $P_{\rm Galaxy}$, and $P_{\rm Star}$ parameters for the classification. As illustrated in Figure 2, a target is classified as a quasar when its $P_{\rm QSO}$ is higher than $P_{\rm Galaxy}$ and $P_{\rm Star}$ (thus, the normalized probability $P_{\rm QSO}$ in Equation (10) is larger than one-third). We successfully classify 94.7% of quasars, 99.3% of galaxies, and 96.3% of stars when all bands are available. Fewer quasars are misclassified as stars when including MIR photometry, since stars usually radiate thermal emission and are faint in the MIR. At the faint end, without NIR and/or MIR photometry, more quasars are

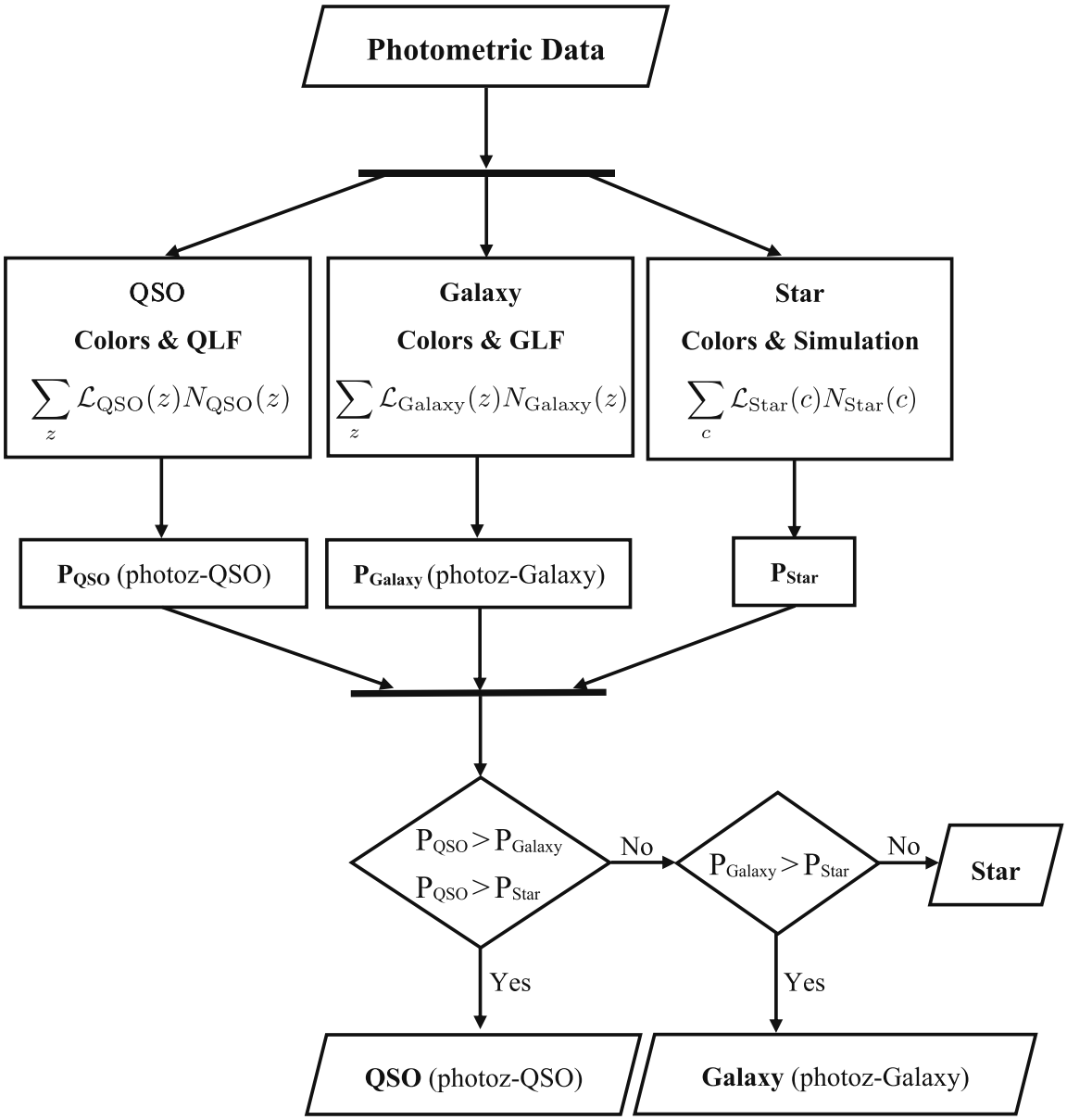

Figure 2. Quasar candidate selection flowchart. For a given object with relative fluxes and magnitudes, we calculate the probability of the object being a quasar, galaxy, or star. We compare these probabilities and classify the candidate into quasar, galaxy, or star. We also obtain photoz-QSO for quasar candidates and photoz-galaxy for galaxy candidates.

misclassified as galaxies due to contamination from their host galaxies.

Figure 4 shows the distribution of *i*-band magnitude for the 102,321 spectroscopically confirmed quasars in the DES footprint, along with our photometric classifications. In this figure, we use all available bands, and 83%, 14%, and 2% of them are classified as quasars, galaxies, and stars, respectively. Quasars at the faint end, especially at $i > 22$, might be misclassified as galaxies.

Stars and galaxies misclassified as quasars will decrease the purity of the selected quasar candidate sample. Using our benchmark sample of spectroscopically confirmed galaxies and stars, only a small fraction (0.1%–0.3%) of stars are misclassified as quasars, and a small fraction (0.2%–0.5%) of galaxies are misclassified as quasars (see Table 3). These contamination rates are based on the loosest quasar selection criteria. Using a higher $P_{\rm QSO}$ cut, the contamination from stars and galaxies can be further reduced. Of course, the absolute contamination fraction depends on the densities of stars and galaxies in the targeting field. In Section 4.2, we show the full selection criteria, as well as the completeness and efficiency (purity) for our quasar selection for typical high-Galactic-latitude fields.

4.2. Quasar Candidates

We now perform quasar target selection over the 5000 deg^2 DES wide-field area. Table 4 summarizes the steps to select quasar candidates. We use the following criteria to optimize the quasar selection.

1. The maximum S/N in five DES bands is greater than 5, SN_MAX_PSF > 5.

Table 3
Regression and Classification Results for Spectroscopically Known Objects

Combination	N_b	QSO						Galaxy						Star			
		N	$R_{0.1}$	$\sigma(\Delta z)$	Q	G	S	N	$R_{0.1}$	$\sigma(\Delta z)$	Q	G	S	N	Q	G	S
DES_YJHK_W1W2	11	33,805	**92.2%**	0.147	**94.7%**	4.9%	0.4%	134,163	**98.1%**	0.035	0.5%	**99.3%**	0.2%	135,975	0.1%	3.6%	**96.3%**
DES_YJHK_W1	10	34,200	**90.9%**	0.157	**91.2%**	6.7%	2.1%	139,134	**97.9%**	0.038	0.5%	**99.2%**	0.3%	144,598	0.1%	2.7%	**97.1%**
DES_JHK_W1W2	10	53,448	**90.7%**	0.157	**92.8%**	6.5%	0.7%	190,258	**97.6%**	0.040	0.4%	**99.2%**	0.4%	176,229	0.1%	4.4%	**95.6%**
DES_JK_W1W2	9	61,477	**89.2%**	0.160	**91.3%**	7.7%	1.0%	207,236	**97.1%**	0.044	0.4%	**99.2%**	0.4%	180,532	0.1%	3.4%	**96.6%**
DES_JHK_W1	9	54,467	**89.2%**	0.164	**87.8%**	9.6%	2.6%	199,921	**97.1%**	0.046	0.5%	**99.2%**	0.4%	187,735	0.1%	4.4%	**95.5%**
DES_YJHK	9	34,601	**88.7%**	0.187	**81.9%**	13.7%	4.4%	141,975	**96.9%**	0.045	0.4%	**99.2%**	0.5%	147,780	0.2%	4.4%	**95.4%**
DES_JK_W1	8	62,875	**87.7%**	0.170	**85.8%**	11.2%	3.0%	219,002	**96.3%**	0.051	0.4%	**99.2%**	0.5%	193,026	0.1%	3.0%	**96.9%**
DES_J_W1W2	8	69,830	**87.2%**	0.169	**89.0%**	10.4%	0.6%	214,337	**96.1%**	0.051	0.3%	**99.3%**	0.4%	181,408	0.1%	3.1%	**96.8%**
DES_JHK	8	55,462	**86.0%**	0.201	**76.3%**	17.5%	6.2%	204,590	**95.9%**	0.053	0.4%	**99.1%**	0.5%	192,853	0.1%	14.6%	**85.3%**
DES_W1W2	7	86,947	**85.5%**	0.166	**81.9%**	17.6%	0.5%	237,998	**93.9%**	0.067	0.2%	**99.2%**	0.6%	182,659	0.1%	3.8%	**96.1%**
DES_J_W1	7	72,748	**84.6%**	0.184	**82.4%**	15.8%	1.8%	233,336	**94.9%**	0.060	0.4%	**99.1%**	0.5%	195,228	0.1%	1.6%	**98.3%**
DES_JK	7	64,192	**83.9%**	0.208	**73.5%**	18.2%	8.3%	224,375	**95.2%**	0.058	0.3%	**99.0%**	0.7%	198,569	0.1%	3.8%	**96.1%**
DES_W1	6	94,277	**82.8%**	0.179	**70.7%**	27.9%	1.4%	292,647	**91.5%**	0.080	0.3%	**99.1%**	0.6%	197,247	0.2%	2.0%	**97.8%**
DES_J	6	75,397	**77.3%**	0.244	**57.8%**	23.1%	19.1%	241,349	**93.6%**	0.068	0.2%	**98.6%**	1.2%	208,799	0.2%	3.3%	**96.5%**
DES	5	102,321	**72.2%**	0.273	**40.6%**	42.3%	17.1%	318,138	**90.0%**	0.085	0.2%	**98.2%**	1.6%	219,857	0.3%	7.2%	**92.5%**

Note. Here N_b is the number of bands; N is the number of objects; $R_{0.1}$ is the fraction of objects with $|\Delta z|$ smaller than 0.1, where $\Delta z = (z_s - z_p)/(1 + z_s)$; and $\sigma(\Delta z)$ is the standard deviation of Δz. The columns "Q," "G," and "S" stand for fractions of objects classified as quasars, galaxies, and stars. The table is ranked by the $R_{0.1}$ value of QSO (from high to low). As a visual aid, we use bold to highlight the most useful columns (larger values better).

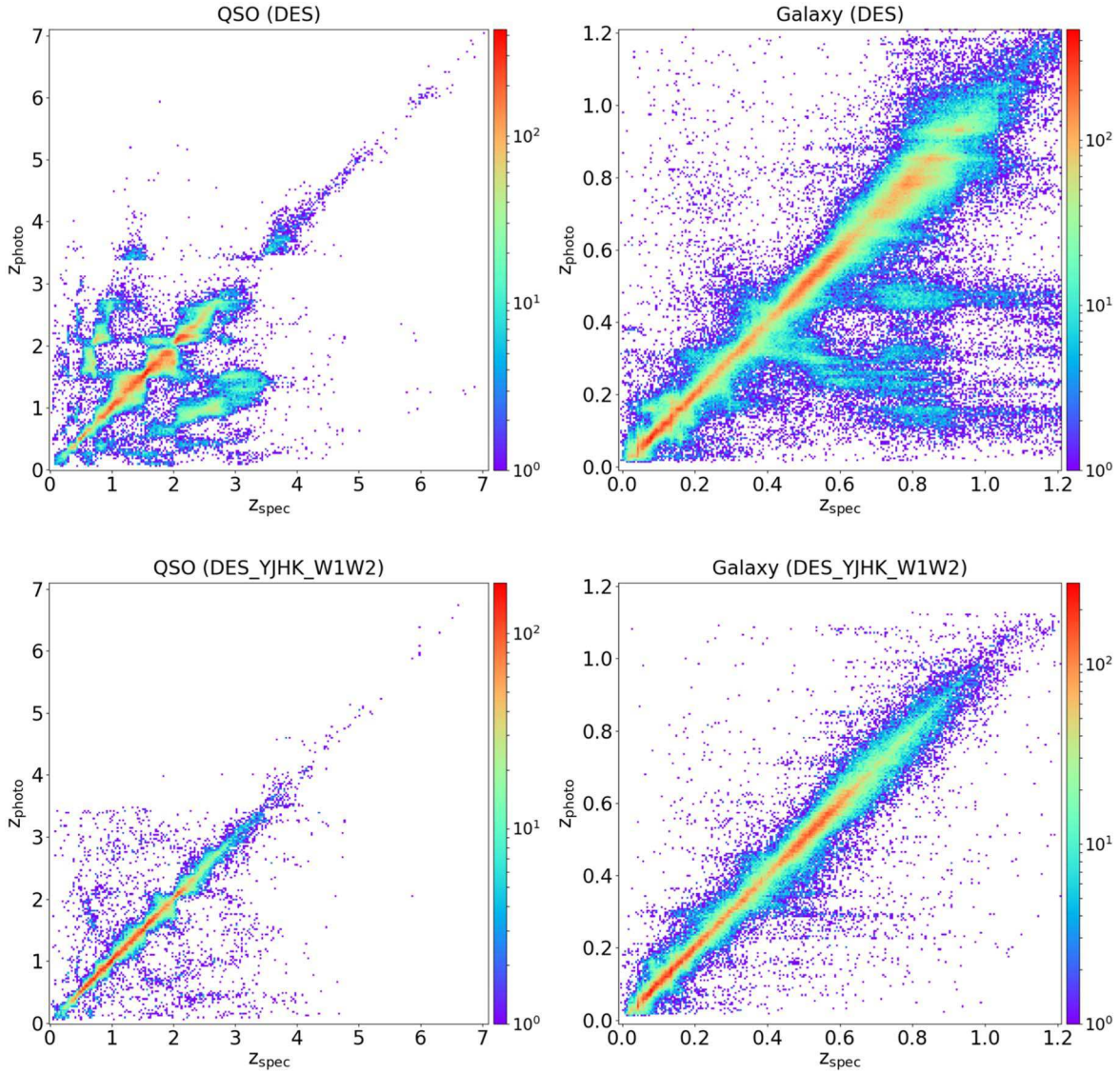

Figure 3. Comparison between photo-zs and the spectroscopic redshifts for quasars (left panels) and galaxies (right panels). The top panels show the results with the fewest bands, only using five-band DES photometry; the bottom panels show the results with the most bands, using all available photometry from optical, NIR, and MIR (i.e., the DES_YJHK_W1W2 combination). The color map indicates the source number at each grid point. For quasars, there is a degeneracy between $z \sim 0.8$ and 2–3, and this problem is alleviated by combining optical data with infrared photometry.

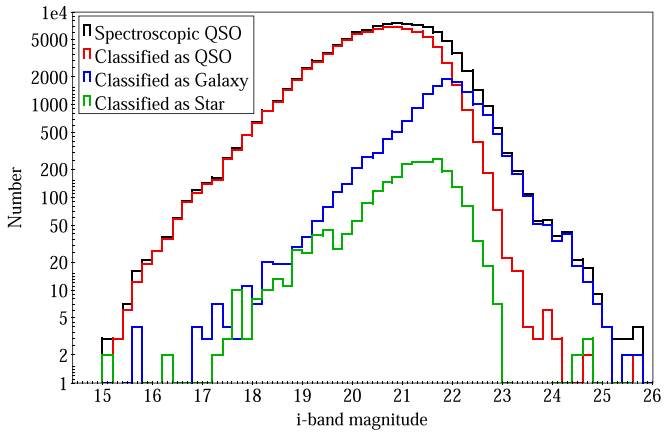

Figure 4. Distribution of i-band magnitudes for spectroscopically known quasars (black). The red, blue, and green lines are sources classified as quasars, galaxies, and stars, respectively. The y-axis is in logarithmic scale.

2. At least two DES bands have an S/N greater than 3, SN3 > 2 .
3. We request a baseline quality criterion of IMAFLAGS_ISO $= 0$ in all DES bands.
4. The Gaia proper-motion significance, PMSIG, and parallax significance, PLXSIG, are smaller than 5.
5. The skewt-QSO probability of quasars, $P_{\rm QSO}$, is larger than those of stars, $P_{\rm Star}$, and galaxies, $P_{\rm Galaxy}$, i.e., $P_{\rm QSO} > P_{\rm Star}$ and $P_{\rm QSO} > P_{\rm Galaxy}$; thus, $P_{\rm QSO} > 1/3$ by construction.

In total, there are 691,483,608 sources in the DES DR2 coadded photometric catalog. Among these sources, there are 1.47, 645.88, and 44.13 million sources classified as quasars, galaxies, and stars, respectively, using the skewt-QSO probabilities only (i.e., criterion (5)). Using criteria (1)–(5) above, we photometrically classify 1,352,947 as quasar candidates, 334,484,173 as galaxy candidates, and 36,950,258 as star candidates (criterion (4) was not applied to star candidates).

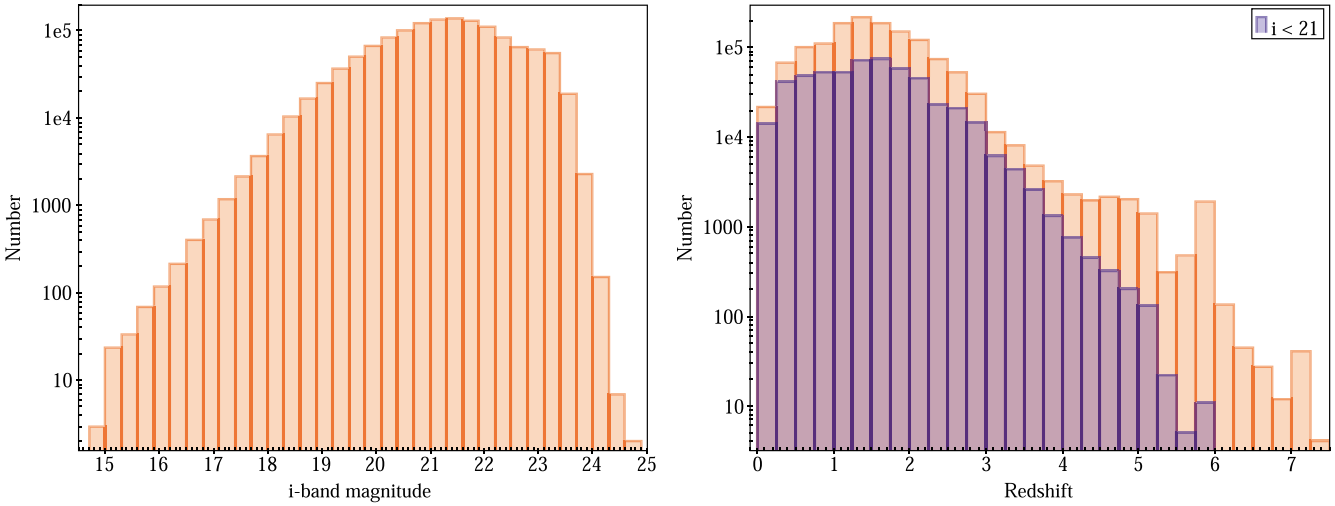

Figure 5. Distributions of i-band magnitudes (left panel) and photometric redshifts (right panel) of the 1,352,947 quasar candidates in the DES wide footprint. The y-axes are in logarithmic scales. The blue histogram in the right panel shows quasar candidates with $i < 21$.

Table 4
QSO Selection Criteria

Criteria		Candidates		Known QSOs in DES DR2	
		All	$P_{\rm QSO} > P_{\rm Star}$ and $P_{\rm QSO} > P_{\rm Galaxy}$	All	$i < 21.5$
All		691,483,608 (100%)	1,471,001 (100%)	102,321 (100%)	84,280 (100%)
SN_MAX_PSF > 5	(1)	391,279,183 (56.6%)	1,402,955 (95.4%)	102,173 (99.9%)	84,174 (99.9%)
SN3 > 2	(2)	375,038,065 (54.2%)	1,375,613 (93.5%)	102,162 (99.8%)	84,174 (99.9%)
IMAFLAGS_ISO = 0	(3)	372,958,657 (53.9%)	1,358,057 (92.3%)	101,890 (99.6%)	83,966 (99.6%)
PLXSIG<5 and PMSIG<5	(4)	358,069,257 (51.8%)	1,352,947 (92.2%)	101,706 (99.4%)	83,782 (99.4%)
$P_{\rm QSO} > P_{\rm Star}$ and $P_{\rm QSO} > P_{\rm Galaxy}$	(5)	1,352,947 (0.196%)	1,352,947 (92.2%)	84,978 (83.1%)	76,424 (90.7%)
$P_{\rm QSO} > 0.7$	(6)	945,860 (0.137%)	945,860 (64.3%)	79,811 (78.0%)	73,802 (87.6%)

Note. We use criteria (1)–(5) for our fiducial quasar catalog, which includes 1,352,947 quasar candidates (see Section 4.2 for details on the criteria). Since $P_{\rm QSO} + P_{\rm Star} + P_{\rm Galaxy} = 1$, criterion (5) implies $P_{\rm QSO} > 1/3$. For a high-completeness selection, we recommend using our fiducial quasar catalog, selected with criteria (1)–(5). For a higher-efficiency (purity) selection while maintaining a high completeness (<85% at $i < 21.5$), we recommend adding criterion (6) of $P_{\rm QSO} > 0.7$. Each selection step also includes all previous criteria. The percentages in parentheses are the fractions of objects among the full sample.

Figure 5 shows the i-band magnitude and redshift distributions of the 1.35 million quasar candidates. In both panels, the y-axes are in logarithmic scale. The left panel shows that the targets are highly complete at $i < 21$ with the log-linear number increasing from bright to faint magnitude. In the right panel, the redshift distribution peaks around 1.5. The QLF studies show that the number density of luminous quasars peaks between redshifts 2 and 3 (e.g., Richards et al. 2006). For quasars with the same absolute magnitude, the apparent magnitude becomes fainter as redshift increases, and in the fainter regime, the selection completeness decreases, so the redshift peak moves toward lower redshift. The blue histogram in the right panel shows the quasar candidates with $i < 21$. With higher completeness at $i < 21$, the redshift distribution between 0.5 and 2.2 becomes flatter, and the peak moves slightly to higher redshift. There are few $z > 6$ quasar candidates with $i > 21$, as the Lyα emission line drops out of the i band at $z > 6$.

Among the set of selection criteria, the first criterion excludes 43.4% of DES sources. The second, third, and fourth criteria further exclude 4.8% of DES sources. The most crucial criterion is the fifth criterion from the skewt-QSO probability, excluding 51.6% of DES sources. Quasars are normally pointlike sources, but low-redshift and faint quasars can be extended sources. Therefore, we did not perform any morphological cuts based on DES imaging.

For higher selection efficiency (purity), we can adopt higher $P_{\rm QSO}$ thresholds. We tested the completeness and efficiency (purity) of quasar selection in the Stripe 82 (S82) region of SDSS, where the spectroscopic completeness of photometric objects is relatively high. Specifically, we use the S82 region with R.A. $< 45°$ or $>317°$ and $|\text{decl.}| < 1.^{\circ}25$. Since the completeness and efficiency vary with magnitude and decrease dramatically at the faint end, here we use quasars brighter than $r = 21.5$, which is appropriate for current spectroscopic quasar surveys. Following Yang et al. (2017), the efficiency (purity) is calculated based on the quasar number estimated from the QLF as

$$\text{efficiency} = \frac{N_{\rm QLF}(r) \times \text{completeness}(r)}{N_{\rm candidates}(r)}, \quad (13)$$

where $N_{\rm QLF}(r)$ is the number of quasars per square degree calculated from the QLF (Palanque-Delabrouille et al. 2016). Figure 6 shows the completeness and efficiency for different

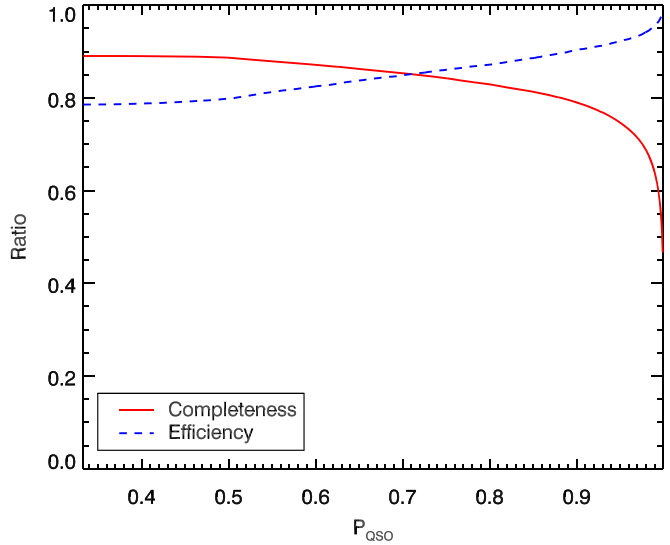

Figure 6. Completeness (red solid line) and efficiency (blue dashed line) as a function of $P_{\rm QSO}$ for spectroscopically confirmed quasars in the S82 region ($r < 21.5$).

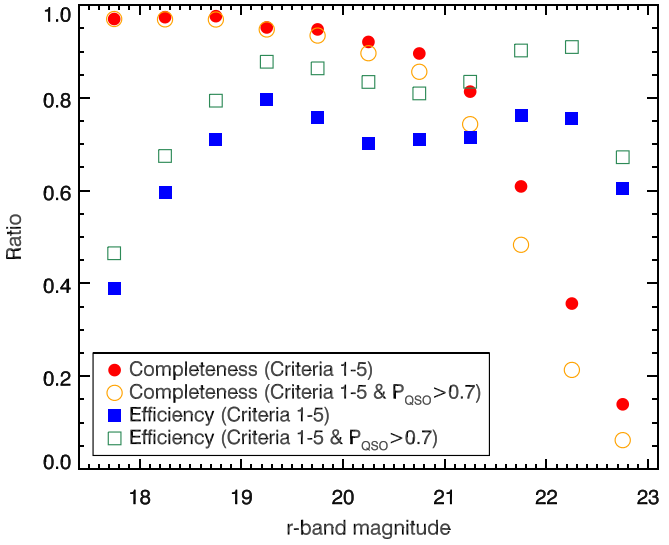

Figure 7. Completeness and efficiency as a function of r-band magnitude using spectroscopically confirmed quasars in the S82 region. The filled red circles and blue squares show results with selection criteria (1)–(5), and the open orange circles and green squares are results with one more criterion, $P_{\rm QSO} > 0.7$.

values of $P_{\rm QSO}$ using the S82 spectroscopically confirmed quasar sample. As we adopt a higher $P_{\rm QSO}$ threshold, the completeness decreases and the efficiency of the selection increases. With our fiducial criteria (1)–(5), there are very few spectroscopically confirmed quasars (0.4%) and quasar candidates (2%) with $1/3 < P_{\rm QSO} \leqslant 0.5$. The completeness and efficiency are both high (∼85%) when using a $P_{\rm QSO}$ threshold of 0.7. Therefore, for a high-completeness selection, we recommend using our fiducial quasar catalog, selected using criteria (1)–(5). For a higher-efficiency selection while maintaining a high completeness (∼85%), we recommend adding one more criterion of $P_{\rm QSO} > 0.7$, which results in 0.95 million quasar candidates.

Figure 7 shows the completeness and efficiency as function of r-band magnitude. The completeness using one more criterion of $P_{\rm QSO} > 0.7$ is lower than that using only criteria (1)–(5), while the efficiency behaves in the opposite sense. The completeness falls below 80% at $r > 21.5$. The drop of efficiency (purity) at the bright end is mainly due to enhanced contamination from misclassified low-redshift bright galaxies. Our algorithm can select some weak- or narrow-line AGNs. For example, among 5741 narrow-line AGNs in the Million Quasars Catalog (type = K or N, i.e., narrow-line quasars or Seyferts) within the DES footprint, our algorithm selects 492 of them. Therefore, the completeness will increase and the contamination rate will decrease if we include narrow-line objects in our quasar selection. On the other hand, the measurements of the QLF are generally difficult at the bright end given the rapid decrease in the spatial density of quasars toward high luminosities. Therefore, our estimated efficiency at the bright end is highly impacted by the quality of the QLF measurement.

Of course, the efficiency of quasar selection also depends on the field stellar density. In sky regions with high stellar densities, the purity will decrease, as more stars will be misclassified as quasars (even if the fraction of stars misclassified as quasars is as low as 0.1%).

We also tested applying the most crucial criterion from the skewt-QSO probability first, resulting in 1.47 million quasar candidates (2.14% of all sources in DES DR2). The other criteria further rule out 0.017% (118,054) sources, demonstrating that $P_{\rm QSO}$ is the most useful parameter to rule out contamination. The Gaia astrometry criteria rule out 5110 additional sources. In the bright regime, where Gaia detects proper motion, 4375 out of 536,956 sources are rejected at $i < 21$. This confirms that our skewt-QSO probability criterion selects very few stellar contaminants with large parallaxes/proper motions. Of course, our photometric quasar sample may still contain many faint stars without reliable Gaia DR2 astrometry.

Using probability distributions of parallax/proper motion as a prior probability or machine-learning approaches as in Shu et al. (2019) will make better use of Gaia astrometric information. However, as shown in Table 4, the skewt-QSO color selection has already ruled out the majority of stars, and using the additional parallax/proper-motion cuts of PMSIG < 5 and PLXSIG < 5 only rules out <0.1% of additional sources of the 1.35 million quasar candidates after the skewt-QSO criteria. In that sense, more refined parallax/proper-motion cuts are unnecessary, since the primary selection of our quasar candidates is the skewt-QSO color selection.

In Table 4, we also list the number of spectroscopically confirmed quasars in the DES DR2 source catalog that pass our selection criteria. Criteria (1)–(5) recover 83.1% (90.7%) of all ($i < 21.5$) spectroscopically confirmed quasars. Using $P_{\rm QSO} > 0.7$, the completeness is 78.0% (87.6%) for all ($i < 21.5$) quasars.

We provide probabilities of quasars, galaxies, and stars for the entire DES DR2 coadded photometric catalog, which contains a total of 691,483,608 sources. The format of our final catalogs is described in Table 5 for the ∼1.4 million quasar candidates and Table 8 for the full DES DR2 source catalog. These catalogs can be downloaded.[9]

[9] http://quasar.astro.illinois.edu/paper_data/DES_QSO/

Table 5
FITS Table Format for DES DR2 Skewt-QSO Catalog

Column Name	Format	Units	Description
COADD_OBJECT_ID	LONG64		Unique identifier for the coadded objects
ALPHAWIN_J2000	DOUBLE	deg	DES R.A. (J2000)
DELTAWIN_J2000	DOUBLE	deg	DES decl. (J2000)
EXTENDED_COADD	INT		DES morphological object classification variable 0: high confidence pointed-like; 1: likely pointed-like; 2: likely extended; 3: high confidence extended
SN_MAX_PSF	FLOAT		Max. S/N of the PSF mag in DES
SN3	INT		Number of bands in DES with S/N higher than 3
Photometry	STRING		DES photometry fitting to quasar and star models, PSF or AUTO
Band_DES	STRING		DES bands
MAG_PSF_GRIZY	FLOAT	mag	DES PSF magnitudes in *grizY* bands
MAGERR_PSF_GRIZY	FLOAT	mag	DES PSF magnitude uncertainties in *grizY* bands
MAG_AUTO_GRIZY	FLOAT	mag	DES AUTO magnitude in *grizY* bands
MAGERR_AUTO_GRIZY	FLOAT	mag	DES AUTO magnitude uncertainties in *grizY* bands
IMAFLAGS_ISO_GRIZY	INT		DES flag in *grizY* bands
PLXSIG	FLOAT		Gaia DR2 parallax significance
PMSIG	FLOAT		Gaia DR2 proper-motion significance
Separation_Gaia	FLOAT	arcsec	Angular distance between DES and Gaia coordinates
CNT9	INT		Number of sources with a 9″ radius circular aperture
DIST	FLOAT	arcsec	Angular distance to the closest neighbor within 9″
Survey_NIR	STRING		NIR survey
Band_NIR	STRING		NIR bands
Nband_NIR	INT		Number of NIR bands
Separation_NIR	FLOAT	arcsec	Angular distance between DES and NIR coordinates
Mag_YJHK	FLOAT	mag	NIR magnitudes in *YJHK* bands (AB magnitude)
Magerr_YJHK	FLOAT	mag	NIR magnitude uncertainties in *YJHK* bands
Band_WISE	STRING		WISE bands (only use W1 and W2 bands)
Nband_WISE	INT		Number of WISE bands
Separation_WISE	FLOAT	arcsec	Angular distance between DES and unWISE coordinates
Mag_W1W2	FLOAT	mag	WISE magnitudes in W1 and W2 bands (AB magnitude)
Magerr_W1W2	FLOAT	mag	WISE magnitude uncertainties in W1 and W2 bands
Combination	STRING		DES, NIR, and MIR band combination
Reference_Band	STRING		DES reference band
*P*_QSO	FLOAT		$P_{\rm QSO}$, skewt-QSO probability fitting to QSO models, described in Equation (10)
photoz_QSO	FLOAT		Quasar photo-z
$z1$_QSO	FLOAT		Lower limit of quasar photo-z
$z2$_QSO	FLOAT		Upper limit of quasar photo-z
*P*_QSO_z	DOUBLE		Probability of quasar photo-z locating within ($z1_{\rm QSO}$, $z2_{\rm QSO}$), described in Equation (5)
*P*_Galaxy	FLOAT		$P_{\rm Galaxy}$, skewt-QSO probability fitting to galaxy models
photoz_Galaxy	FLOAT		Galaxy photo-z
$z1$_Galaxy	FLOAT		Lower limit of galaxy photo-z
$z2$_Galaxy	FLOAT		Upper limit of galaxy photo-z
*P*_Galaxy_z	DOUBLE		Probability of galaxy photo-z locating within ($z1_{\rm Galaxy}$, $z2_{\rm Galaxy}$), described in Equation (7)
*P*_Star	FLOAT		$P_{\rm Star}$, skewt-QSO probability fitting to star models
z_spec	DOUBLE		Spectroscopic redshift, if available
z_spec_cat	STRING		Spectroscopic redshift catalog, i.e., SDSS, Milliquas, or LAMOST
Class_spec	STRING		Spectroscopic classification

5. Discussion

5.1. 2D Completeness in the Magnitude–Redshift Space

Using spectroscopically confirmed quasars, we further quantify our quasar selection completeness as a function of both magnitude and redshift. As shown in Yang et al. (2017), the photometric redshift accuracy and the classification success rate of the skewt-QSO algorithm are high even when using different training and testing samples.

Figure 8 shows the completeness as a function of *i*-band magnitude (left panels) and redshift (right panels) using spectroscopically confirmed quasars. The black diamonds/lines represent the selection results using our fiducial criteria (1)–(5). The blue circles/lines represent the results using one more criterion of $P_{\rm QSO} > 0.7$. The completeness is higher than 80% at $i < 21$ for both selections. The completeness decreases rapidly at $i > 21$, which is the consequence of decreasing photometric accuracy and the lack of infrared detection at the faint end. The right panel in Figure 8 shows the completeness as a function of redshift for $i < 21$ quasars. The overall completeness is >80% for quasars over $0.5 < z < 3$. At the low-redshift end ($z < 1$), the selection completeness decreases as redshift decreases, which is due to enhanced contamination from bright host galaxies of quasars at low redshift that causes the quasar not to be selected based on color. At high redshift ($z > 2.5$), the completeness decreases with redshift. At $z > 3$, the completeness estimation suffers from the small spectroscopic sample size, so we use a larger redshift bin of 0.4 at

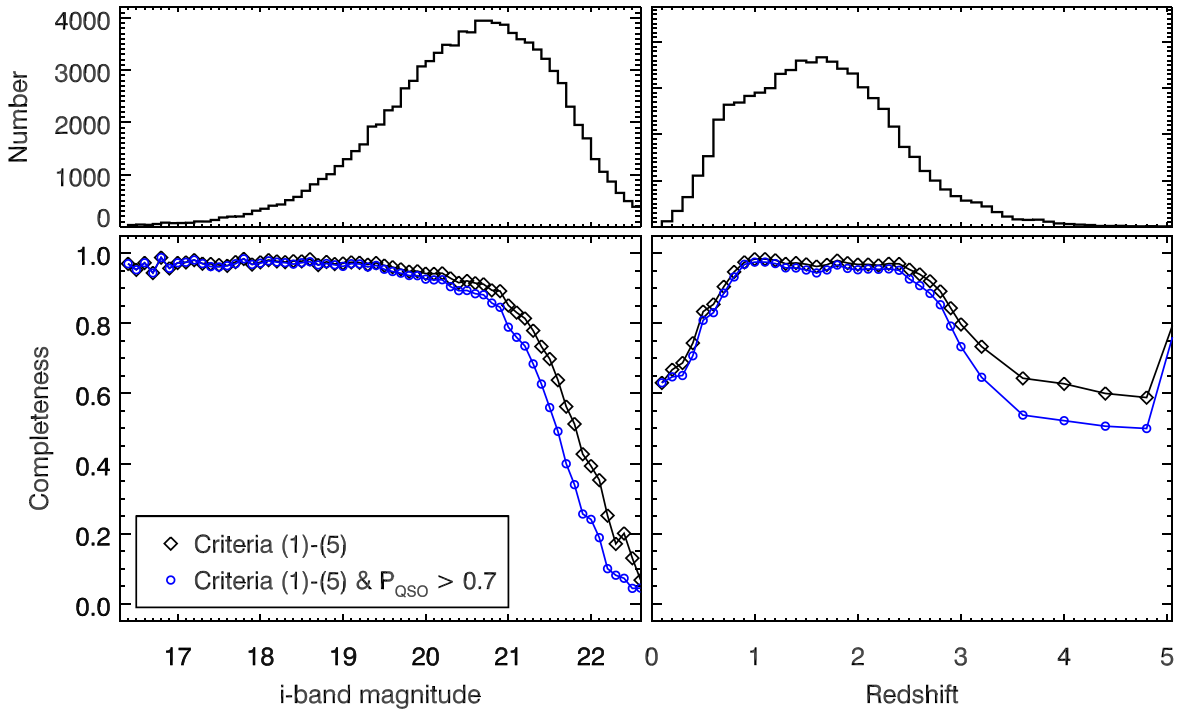

Figure 8. Completeness as a function of *i*-band magnitude (left panels) and redshift (right panels) for spectroscopically confirmed quasars. The top panels show the number distribution. The black diamonds/lines show the results from criteria (1)–(5). The blue circles/lines represent results from criteria (1)–(6).

$z > 3$, comparing to a bin of 0.1 at $z < 3$, to avoid large fluctuations. In addition, these completeness estimates are based on spectroscopically confirmed quasars, thus suffering from their own selection effects and incompleteness. So the total completeness might be even lower than our estimation from the spectroscopic sample, especially at the faint end, where the original spectroscopic sample suffers the most from incompleteness in selection.

We use simulated quasars to remedy the small sample size of real quasars at high redshift. The simulation procedure is described in Section 2.2. We quantify the selection completeness using a sample of ∼0.8 million simulated quasars spanning a wide range of redshifts and magnitudes. Figure 9 shows the 2D completeness as a function of redshift (*x*-axis) and *i*-band magnitude (*y*-axis) using $P_{\rm QSO} > P_{\rm Galaxy}$ and $P_{\rm QSO} > P_{\rm Star}$, color-coded by selection completeness. The solid cyan line shows the location where the completeness is ∼80%. Figure 9 confirms that at low redshift ($z < 1$), the completeness decreases with decreasing redshift due to increasing host galaxy contamination. At $z > 3.3$, the completeness does not decrease with redshift, indicating that the trend observed in Figure 8 is mainly due to the small sample statistics at high redshift. At $z > 1$, the completeness is roughly constant and starts to decrease with increasing magnitude around $i \sim 21$–22. At certain redshifts, for example, $z \sim 1.8$, 3.0, 4.8, and 5.5, the 80% selection completeness is achieved at a shallower magnitude limit due to contamination from different types of stars with decreasing effective temperatures.

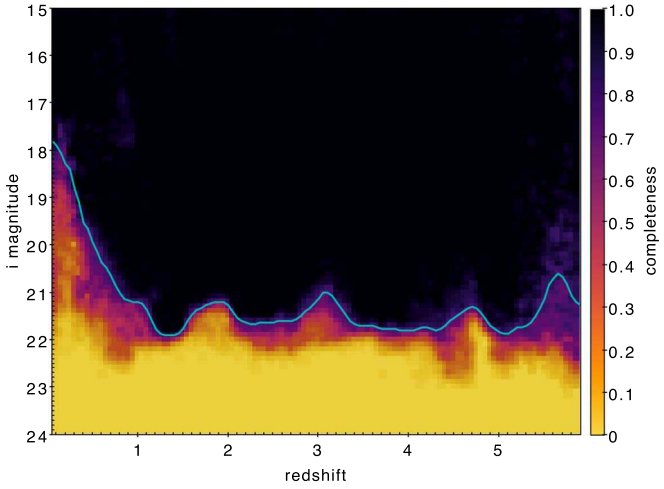

Figure 9. The 2D selection completeness map as a function of redshift (*x*-axis) and *i*-band magnitude (*y*-axis) using criteria $P_{\rm QSO} > P_{\rm Galaxy}$ and $P_{\rm QSO} > P_{\rm Star}$ on a sample of simulated quasars. The color indicates the completeness. The solid cyan line shows the location where the completeness is 80%.

5.2. Comparison to Gaia QSOC Redshifts

The Gaia DR3 release includes redshift estimates for extragalactic sources using low-resolution BP/RP spectra (Gaia Collaboration et al. 2022). In Gaia DR3, the Quasi Stellar Object Classifier (QSOC) systematically published redshift predictions for 1,834,118 sources, with a very low threshold on the Discrete Source Classifier quasar probability of classprob_dsc_combmod_quasar $\geqslant 0.01$ and a warning flag of redshift estimation of flags_qsoc $\leqslant 16$ (Delchambre et al. 2022). There are 47,451 spectroscopically confirmed quasars in both our 1.35 million quasar candidate catalog and the 1.8 million Gaia QSOC redshift sample. Figure 10 shows the comparison between photo-*z*s and spectroscopic redshifts for our algorithm (left panel) and the Gaia QSOC redshifts (right panel) for these 47,451 quasars. The photo-*z* accuracy $R_{0.1}$ is 93.4% and 61.1% from our algorithm and Gaia QSOC, respectively. Using photo-*z*s from our algorithm, the vast majority are along the 1:1 line. Gaia QSOC redshifts from the low-resolution spectra have a smaller scatter along the 1:1 line,

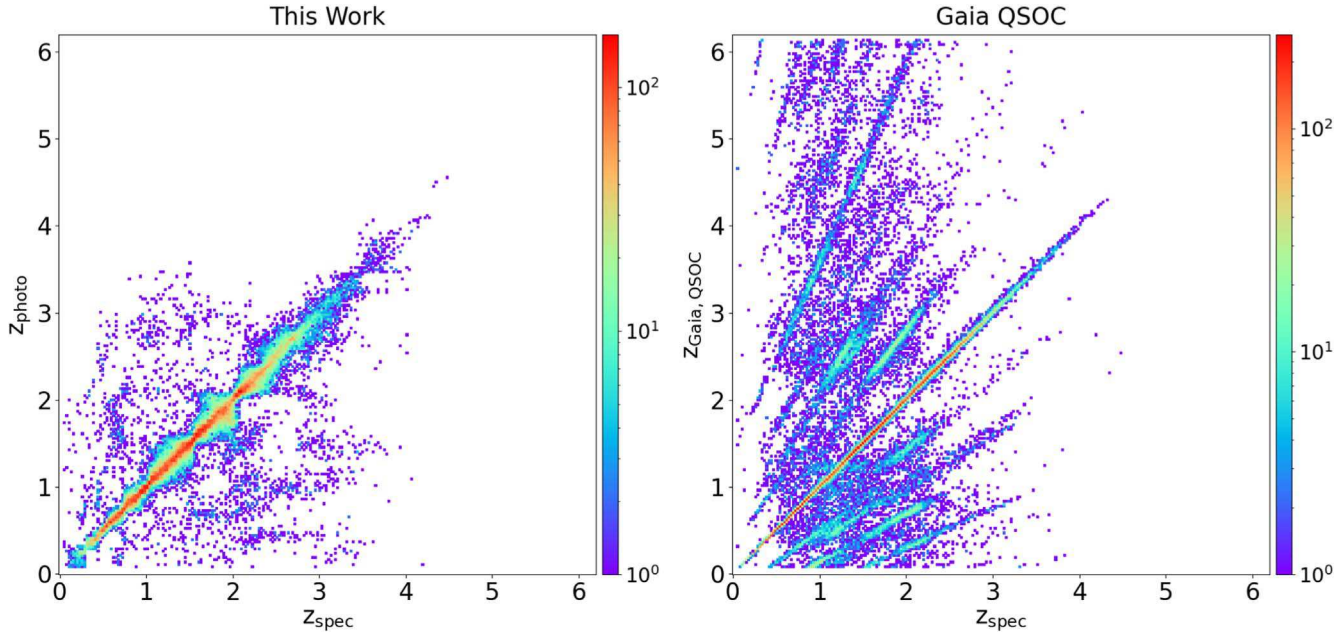

Figure 10. Comparison with the spectroscopic redshifts for our photo-zs (left panel) and Gaia QSOC redshifts (right panel) for 47,451 spectroscopically confirmed quasars covered in both our DES photometric quasar sample and Gaia QSOC. The color map indicates the source number at each grid point. The photo-z accuracy $R_{0.1}$ is 93.4% and 61.1% for our photo-zs and Gaia QSOC redshifts, respectively. Thus, the catastrophic redshift failure rate is much higher for the Gaia QSOC.

indicating smaller redshift uncertainties than our photo-zs (as expected), but there are additional stripes that represent misidentified emission lines in Gaia low-resolution spectra. In particular, 4% of the Gaia QSOC redshifts are incorrectly predicted at $z > 4.6$, grossly overpredicting the abundance of high-redshift quasars. Using a more stringent cut of *flags_qsoc* $= 0$ with empty warning flags, described by Delchambre et al. (2022), the Gaia QSOC redshift accuracy $R_{0.1}$ increases to 95.0%, but the sample is downsized to only 20%. In comparison, using a higher-quality cut in our algorithm of $P\_\mathrm{QSO}\_z > 0.5$, i.e., the integrated probability of the identified photo-z peak is higher than 0.5, our photo-z accuracy $R_{0.1}$ increases to 94.7%, while the sample is only slightly downsized to 95%.

6. Summary

We perform quasar target selection in the southern hemisphere over the ∼5000 deg^2 DES wide survey area. We utilize public DES DR2 optical photometry and available NIR photometric data from various surveys, including VHS, VIKING, UHS, ULAS, and 2MASS. In the MIR, we use the all-sky unWISE photometric data. Our algorithm can efficiently classify sources into the categories of quasars, galaxies, and stars, as well as derive photo-zs for quasar and galaxy candidates.

Our algorithm can successfully classify 94.7% of quasars, 99.3% of galaxies, and 96.3% of stars when all bands are available, benchmarked on spectroscopically confirmed samples. The classification and photo-z success rate decrease when fewer bands are available. The quasar (galaxy) photo-z accuracy $R_{0.1}$, the fraction of objects with $|\Delta z| \equiv |z_s - z_p|/(1 + z_s)$ smaller than 0.1, is as high as 92.2% (98.1%) when all bands are available and decreases to 72.2% (90.0%) when only using five-band photometry from DES.

We select 1.4 million quasar candidates over the DES wide survey footprint and provide all classification probabilities to customarily select quasar samples with different completeness and efficiency (purity). Selection completeness and efficiency are anticorrelated. We recommend using our fiducial criteria (Section 4.2) for the most complete quasar sample. We recommend using one more criterion of $P_{\mathrm{QSO}} > 0.7$ for a higher-purity selection and simultaneous high completeness (∼85%).

We provide our quasar, galaxy, and star probabilities for all ∼0.69 billion sources in the DES DR2 coadd photometric catalog. This catalog will be useful for a broad range of extragalactic and galactic sciences in the southern hemisphere.

Q.Y. and Y.S. acknowledge support from NSF grants AST-1715579 and AST-2009947.

Funding for the DES Projects has been provided by the U.S. Department of Energy, the U.S. National Science Foundation, the Ministry of Science and Education of Spain, the Science and Technology Facilities Council of the United Kingdom, the Higher Education Funding Council for England, the National Center for Supercomputing Applications at the University of Illinois at Urbana-Champaign, the Kavli Institute of Cosmological Physics at the University of Chicago, the Center for Cosmology and Astro-Particle Physics at the Ohio State University, the Mitchell Institute for Fundamental Physics and Astronomy at Texas A&M University, Financiadora de Estudos e Projetos, Fundação Carlos Chagas Filho de Amparo à Pesquisa do Estado do Rio de Janeiro, Conselho Nacional de Desenvolvimento Científico e Tecnológico and the Ministério da Ciência, Tecnologia e Inovação, the Deutsche Forschungsgemeinschaft, and the Collaborating Institutions in the Dark Energy Survey.

The Collaborating Institutions are Argonne National Laboratory, the University of California at Santa Cruz, the University of Cambridge, Centro de Investigaciones Energéticas, Medioambientales y Tecnológicas-Madrid, the University of Chicago, University College London, the DES-Brazil Consortium, the University of Edinburgh, the Eidgenössische

Technische Hochschule (ETH) Zürich, Fermi National Accelerator Laboratory, the University of Illinois at Urbana-Champaign, the Institut de Ciències de l'Espai (IEEC/CSIC), the Institut de Física d'Altes Energies, Lawrence Berkeley National Laboratory, the Ludwig-Maximilians Universität München and the associated Excellence Cluster Universe, the University of Michigan, NSF's NOIRLab, the University of Nottingham, The Ohio State University, the University of Pennsylvania, the University of Portsmouth, SLAC National Accelerator Laboratory, Stanford University, the University of Sussex, Texas A&M University, and the OzDES Membership Consortium.

Based in part on observations at Cerro Tololo Inter-American Observatory at NSF's NOIRLab (NOIRLab Prop. ID 2012B-0001; PI: J. Frieman), which is managed by the Association of Universities for Research in Astronomy (AURA) under a cooperative agreement with the National Science Foundation.

The DES data management system is supported by the National Science Foundation under grant Nos. AST-1138766 and AST-1536171. The DES participants from Spanish institutions are partially supported by MICINN under grants ESP2017-89838, PGC2018-094773, PGC2018-102021, SEV-2016-0588, SEV-2016-0597, and MDM-2015-0509, some of which include ERDF funds from the European Union. IFAE is partially funded by the CERCA program of the Generalitat de Catalunya. Research leading to these results has received funding from the European Research Council under the European Union's Seventh Framework Program (FP7/2007-2013) including ERC grant agreements 240672, 291329, and 306478. We acknowledge support from the Brazilian Instituto Nacional de Ciência e Tecnologia (INCT) do e-Universo (CNPq grant 465376/2014-2).

We acknowledge the use of SDSS data. Funding for SDSS-III has been provided by the Alfred P. Sloan Foundation, the Participating Institutions, the National Science Foundation, and the U.S. Department of Energy Office of Science. The SDSS-III website is http://www.sdss3.org/. The SDSS-III is managed by the Astrophysical Research Consortium for the Participating Institutions of the SDSS-III Collaboration, including the University of Arizona, the Brazilian Participation Group, Brookhaven National Laboratory, Carnegie Mellon University, the University of Florida, the French Participation Group, the German Participation Group, Harvard University, the Instituto de Astrofisica de Canarias, the Michigan State/Notre Dame/JINA Participation Group, Johns Hopkins University, Lawrence Berkeley National Laboratory, the Max Planck Institute for Astrophysics, the Max Planck Institute for Extraterrestrial Physics, New Mexico State University, New York University, Ohio State University, Pennsylvania State University, the University of Portsmouth, Princeton University, the Spanish Participation Group, the University of Tokyo, the University of Utah, Vanderbilt University, the University of Virginia, the University of Washington, and Yale University.

We acknowledge the use of LAMOST data. The Large Sky Area Multi-Object Fiber Spectroscopic Telescope (LAMOST, also named Guoshoujing Telescope) is a National Major Scientific Project built by the Chinese Academy of Sciences. Funding for the project has been provided by the National Development and Reform Commission. LAMOST is operated and managed by the National Astronomical Observatories, Chinese Academy of Sciences.

We acknowledge the use of NIR data, including VHS, VIKING, ULAS, and UHS. The UHS is a partnership between the UK STFC, the University of Hawaii, the University of Arizona, Lockheed Martin, and NASA. This publication makes use of data products from the Two Micron All Sky Survey, which is a joint project of the University of Massachusetts and the Infrared Processing and Analysis Center/California Institute of Technology, funded by the National Aeronautics and Space Administration and the National Science Foundation. This publication makes use of data products from the Wide-field Infrared Survey Explorer, which is a joint project of the University of California, Los Angeles, and the Jet Propulsion Laboratory/California Institute of Technology, funded by the National Aeronautics and Space Administration.

Appendix A
Quasar Targets for the Black Hole Mapper in SDSS-V

We perform quasar target selection for the Black Hole Mapper (BHM) program in SDSS-V (Kollmeier et al. 2017), in particular, targets in the reverberation mapping (RM) fields. We use the same algorithm but utilize additional optical photometric data. Table 6 summarizes the photometric data we use for the seven initial BHM-RM fields. We use DES photometric data in the XMM-LSS, CDFS, EDFS, and ELAIS-S1 fields. We use the Pan-STARRS1 data (Chambers et al. 2016) for the COSMOS and SDSS-RM fields in the northern sky. For the S-CVZ field, we use optical photometric data from Gaia DR2 or the NOAO Source Catalog (NSC; Nidever et al. 2018). In addition, we make use of available NIR data in these fields. We use unWISE W1 and W2 photometric data in all fields. Since there are very few high-redshift (i-band dropouts at $z > 5.8$) quasars in these small fields, we use the i band (or Gaia G band) as the reference band for quasar target selection in these BHM-RM fields. The final quasar target catalog for BHM-RM fields is presented in Table 7. We required the skewt-QSO probability criteria (i.e., $P\_QSO > P\_Star$ and $P\_QSO > P\_Galaxy$ in non-S-CVZ fields and $P\_QSO\_Gaia > P\_Star\_Gaia$ and $P\_QSO\_Gaia > P\_Galaxy\_Gaia$ in the S-CVZ field). The SDSS-V BHM-RM quasar targets (v0.5) were selected from this catalog with further criteria on log_QSO, PLXSIG, PMSIG, and magnitude limits on i-band (or Gaia G-band) magnitude. Specifically, we used a criterion of $\log\_QSO > -10$ for SDSS-V BHM-RM quasar targets (v0.5). This criterion is explained in more detail in Yang et al. (2017).

Table 6
Deep BHM-RM Fields in SDSS-V

Field Name	R.A. Center	Decl. Center	Optical Survey	Infrared Survey
XMM-LSS	02:22:50.00	−04:45:00.0	DES	VHS
CDFS	03:30:35.60	−28:06:00.0	DES	VHS/VIKING/VIDEO
EDFS	04:04:57.84	−48:25:22.8	DES	VHS
ELAIS-S1	00:37:48.00	−44:00:00.0	DES	VHS
COSMOS	10:00:00.00	+02:12:00.0	PS1	LAS
SDSS-RM	14:14:49.00	+53:05:00.0	PS1	UHS
S-CVZ	06:00:00.00	−66:33:38.0	Gaia/NSC	VHS/VMC

Note. VIDEO: VISTA Deep Extragalactic Observations Survey (DR5). VMC: VISTA Magellanic Cloud Survey (DR4).

Table 7
FITS Table Format for Quasar Targets for the BHM-RM Program in SDSS-V

Column Name	Format	Units	Description
FIELD_NAME	STRING		XMM-LSS, CDFS, EDFS, ELAIS-S1, COSMOS, SDSS-RM, or S-CVZ
POS_REF	STRING		Fiducial coordinates reference, priority: Gaia > DES > PS1 > NSC
RA	DOUBLE	deg	Fiducial R.A. (J2000)
DEC	DOUBLE	deg	Fiducial decl. (J2000)
Distance	DOUBLE	deg	Angular distance from the field center
EBV	DOUBLE	mag	Galactic $E(B-V)$ reddening from Schlegel et al. (1998)
DES	INT		A flag set to 1 if in DES photometric catalog
DES_MAG	DOUBLE	mag	DES PSF magnitudes in *grizY* bands
DES_MAGERR	DOUBLE	mag	DES PSF magnitude uncertainties in *grizY* bands
PS1	INT		A flag set to 1 if in PS1 photometric catalog
PS1_MAG	DOUBLE	mag	PS1 PSF magnitudes in *grizy* bands
PS1_MAGERR	DOUBLE	mag	PS1 PSF magnitude uncertainties in *grizy* bands
NSC	INT		A flag set to 1 if in NSC catalog
NSC_MAG	DOUBLE	mag	NSC PSF magnitudes in *grizY* bands
NSC_MAGERR	DOUBLE	mag	NSC PSF magnitude uncertainties in *grizY* bands
SDSS	INT		A flag set to 1 if in SDSS photometric catalog
SDSS_MAG	DOUBLE	mag	SDSS PSF magnitudes in *ugriz* bands
SDSS_MAGERR	DOUBLE	mag	SDSS PSF magnitude uncertainties in *ugriz* bands
Gaia	INT		A flag set to 1 if in Gaia photometric catalog
Gaia_MAG	DOUBLE	mag	Gaia magnitudes in G, $G_{\rm BP}$, and $G_{\rm RP}$ bands
Gaia_MAGERR	DOUBLE	mag	Gaia magnitude uncertainties in G, $G_{\rm BP}$, and $G_{\rm RP}$ bands
PLXSIG	FLOAT		Gaia DR2 parallax significance
PMSIG	FLOAT		Gaia DR2 proper-motion significance
WISE	INT		A flag set to 1 if in WISE photometric catalog
WISE_MAG	DOUBLE	mag	WISE magnitudes in W1 and W2 bands (in Vega magnitude)
WISE_MAGERR	DOUBLE	mag	WISE magnitude uncertainties in W1 and W2 bands
Separation_WISE	FLOAT	arcsec	Angular distance between WISE and the fiducial coordinates
NIR	INT		A flag set to 1 if in NIR photometric catalog
Survey_NIR	STRING		NIR survey
NIR_MAG	DOUBLE	mag	NIR magnitudes in *YJHK* bands (in Vega magnitude)
NIR_MAGERR	DOUBLE	mag	NIR magnitude uncertainties in *YJHK* bands
Separation_NIR	FLOAT	arcsec	Angular distance between NIR and the fiducial coordinates
Optical_Survey	STRING		Optical survey used in skewt-QSO, e.g., DES, PS1, Gaia, NSC
mi	DOUBLE	mag	*i*-band PSF magnitude
Nband_Optical	INT		Number of optical bands used in skewt-QSO
Combination	STRING		Optical, NIR, and MIR survey combination
log_QSO	DOUBLE		Natural logarithmic probability of a target fitting to QSO (Equation (9))
*P*_QSO	FLOAT		$P_{\rm QSO}$, skewt-QSO probability fitting to QSO models, described in Equation (10)
*P*_Galaxy	FLOAT		$P_{\rm Galaxy}$, skewt-QSO probability fitting to galaxy models
*P*_Star	FLOAT		$P_{\rm Star}$, skewt-QSO probability fitting to star models
*P*_QSO_Gaia	FLOAT		*P*_QSO using Gaia/NSC photometric data (for the S-CVZ field)
*P*_Galaxy_Gaia	FLOAT		*P*_Galaxy using Gaia/NSC photometric data (for the S-CVZ field)
*P*_Star_Gaia	FLOAT		*P*_Star using Gaia/NSC photometric data (for the S-CVZ field)
photoz_QSO	FLOAT		Quasar photo-z
$z1$_QSO	FLOAT		Lower limit of quasar photo-z
$z2$_QSO	FLOAT		Upper limit of quasar photo-z
*P*_QSO_z	DOUBLE		Probability of quasar photo-z locating within ($z1_{\rm QSO}$, $z2_{\rm QSO}$), described in Equation (5)

Appendix B
A Catalog for All DES DR2 Sources

We publicly release our quasar, galaxy, and star probabilities for all (0.69 billion) photometric sources in the DES DR2 coadded source catalog. We assign photo-z and probability parameters as those of quasars when $P_{\rm QSO} > P_{\rm Galaxy}$ and galaxies when $P_{\rm QSO} \leqslant P_{\rm Galaxy}$. The last three columns in Table 8 are the probabilities that only use likelihood; i.e., no prior probabilities were used in Equation (8). These likelihood parameters are useful for redshift ranges where the luminosity functions may not be well measured, for example, for high-redshift quasars at $z > 6$.

Table 8
FITS Table Format for All DES DR2 Sources

Column	Format	Units	Description
COADD_OBJECT_ID	LONG64		Unique identifier for the coadded objects
ALPHAWIN_J2000	DOUBLE	deg	DES R.A. (J2000)
DELTAWIN_J2000	DOUBLE	deg	DES decl. (J2000)
EXTENDED_COADD	INT		DES morphological object classification variable 0: high confidence pointed-like; 1: likely pointed-like; 2: likely extended; 3: high confidence extended
SN_MAX_PSF	FLOAT		Max S/N of the PSF mag in DES
SN3	INT		Number of bands in DES with S/N higher than 3
Photometry	STRING		DES photometry fitting to quasar and star models, PSF or AUTO
Band_DES	STRING		DES bands
Reference_Band	STRING		DES reference band
IMAFLAGS_ISO_GRIZY	INT		DES flag in *grizY* bands
PLXSIG	FLOAT		Gaia parallax significance
PMSIG	FLOAT		Gaia proper-motion significance
Separation_Gaia	FLOAT	arcsec	Angular distance between DES and Gaia coordinates
CNT9	INT		Number of sources with a 9″ radius circular aperture
DIST	FLOAT	arcsec	Angular distance to the closest neighbor within 9″
Survey_NIR	STRING		NIR survey
Band_NIR	STRING		NIR bands
Band_WISE	STRING		WISE bands (only use W1 and W2 bands)
Separation_WISE	FLOAT	arcsec	Angular distance between DES and unWISE coordinates
Combination	STRING		DES, NIR, and MIR band combination
Class	STRING		Classification from skewt-QSO probabilities: "QSO," "Galaxy," or "Star"
*P*_Star	FLOAT		Same as $P_{\rm Star}$ in Table 5
Class_photoz	STRING		photo-z class: "QSO" when $P_{\rm QSO} > P_{\rm Galaxy}$; "Galaxy" when $P_{\rm QSO} \leqslant P_{\rm Galaxy}$
P	FLOAT		$P_{\rm QSO}$ when $P_{\rm QSO} > P_{\rm Galaxy}$; $P_{\rm Galaxy}$ when $P_{\rm QSO} \leqslant P_{\rm Galaxy}$
photoz	FLOAT		photoz-QSO when $P_{\rm QSO} > P_{\rm Galaxy}$; photoz-Galaxy when $P_{\rm QSO} \leqslant P_{\rm Galaxy}$
$z1$	FLOAT		$z1_{\rm QSO}$ when $P_{\rm QSO} > P_{\rm Galaxy}$; $z1_{\rm Galaxy}$ when $P_{\rm QSO} \leqslant P_{\rm Galaxy}$
$z2$	FLOAT		$z2_{\rm QSO}$ when $P_{\rm QSO} > P_{\rm Galaxy}$; $z2_{\rm Galaxy}$ when $P_{\rm QSO} \leqslant P_{\rm Galaxy}$
P textsubscriptz	FLOAT		$P_{{\rm QSO}z}$ when $P_{\rm QSO} > P_{\rm Galaxy}$; $P_{{\rm Galaxy}z}$ when $P_{\rm QSO} \leqslant P_{\rm Galaxy}$
Class_other	STRING		Other class: "Galaxy" when $P_{\rm QSO} > P_{\rm Galaxy}$; "QSO" when $P_{\rm QSO} \leqslant P_{\rm Galaxy}$
*P*_other	FLOAT		$P_{\rm Galaxy}$ when $P_{\rm QSO} > P_{\rm Galaxy}$; $P_{\rm QSO}$ when $P_{\rm QSO} \leqslant P_{\rm Galaxy}$
photoz_other	FLOAT		photoz-Galaxy when $P_{\rm QSO} > P_{\rm Galaxy}$; photoz-QSO when $P_{\rm QSO} \leqslant P_{\rm Galaxy}$
$z1$_other	FLOAT		$z1_{\rm Galaxy}$ when $P_{\rm QSO} > P_{\rm Galaxy}$; $z1_{\rm QSO}$ when $P_{\rm QSO} \leqslant P_{\rm Galaxy}$
$z2$_other	FLOAT		$z2_{\rm Galaxy}$ when $P_{\rm QSO} > P_{\rm Galaxy}$; $z2_{\rm QSO}$ when $P_{\rm QSO} \leqslant P_{\rm Galaxy}$
P textsubscriptz_other	FLOAT		$P_{{\rm Galaxy}z}$ when $P_{\rm QSO} > P_{\rm Galaxy}$; $P_{{\rm QSO}z}$ when $P_{\rm QSO} \leqslant P_{\rm Galaxy}$
*P*_QSO_likelihood	FLOAT		$P_{\rm QSO}$ that only use likelihood
*P*_Galaxy_likelihood	FLOAT		$P_{\rm Galaxy}$ that only use likelihood
*P*_Star_likelihood	FLOAT		$P_{\rm Star}$ that only use likelihood

ORCID iDs

Qian Yang https://orcid.org/0000-0002-6893-3742
Yue Shen https://orcid.org/0000-0003-1659-7035

References

Abbott, T. M. C., Abdalla, F. B., Allam, S., et al. 2018, ApJS, 239, 18
Abbott, T. M. C., Adamów, M., Aguena, M., et al. 2021, ApJS, 255, 20
Ahumada, R., Prieto, C. A., Almeida, A., et al. 2020, ApJS, 249, 3
Bañados, E., Venemans, B. P., Mazzucchelli, C., et al. 2018, Natur, 553, 473
Baldwin, J. A. 1997, in ASP Conf. Ser. 113, IAU Colloq. 159: Emission Lines in Active Galaxies: New Methods and Techniques, ed. B. M. Peterson, F.-Z. Cheng, & A. S. Wilson (San Francisco, CA: ASP), 80
Best, W. M. J., Magnier, E. A., Liu, M. C., et al. 2018, ApJS, 234, 1
Borchers, H. W. 2022, pracma: Practical Numerical Math Functions, R package v2.4.2, CRAN
Bovy, J., Hennawi, J. F., Hogg, D. W., et al. 2011, ApJ, 729, 141
Bovy, J., Myers, A. D., Hennawi, J. F., et al. 2012, ApJ, 749, 41
Calderone, G., Boutsia, K., Cristiani, S., et al. 2019, ApJ, 887, 268
Chambers, K. C., Magnier, E. A., Metcalfe, N., et al. 2016, arXiv:1612.05560
Croom, S. M., Smith, R. J., Boyle, B. J., et al. 2004, MNRAS, 349, 1397
Croom, S. M., Richards, G. T., Shanks, T., et al. 2009, MNRAS, 399, 1755
Dawson, K. S., Schlegel, D. J., Ahn, C. P., et al. 2013, AJ, 145, 10
Delchambre, L., Bailer-Jones, C. A. L., Bellas-Velidis, I., et al. 2022, arXiv:2206.06710
Dye, S., Lawrence, A., Read, M. A., et al. 2018, MNRAS, 473, 5113
Edge, A., Sutherland, W., Kuijken, K., et al. 2013, Msngr, 154, 32
Flesch, E. W. 2019, arXiv:1912.05614
Gaia Collaboration, Mignard, F., Klioner, S. A., et al. 2018a, A&A, 616, A14
Gaia Collaboration, Brown, A. G. A., Vallenari, A., et al. 2018b, A&A, 616, A1
Gaia Collaboration, Bailer-Jones, C. A. L., Teyssier, D., et al. 2022, arXiv:2206.05681
Hambly, N. C., Collins, R. S., Cross, N. J. G., et al. 2008, MNRAS, 384, 637
Hennawi, J. F., Prochaska, J. X., Burles, S., et al. 2006a, ApJ, 651, 61
Hennawi, J. F., Strauss, M. A., Oguri, M., et al. 2006b, AJ, 131, 1
Hennawi, J. F., Myers, A. D., Shen, Y., et al. 2010, ApJ, 719, 1672
Hopkins, P. F., Richards, G. T., & Hernquist, L. 2007, ApJ, 654, 731
Ivezić, Z. ˇ, Kahn, S. M., Tyson, J. A., et al. 2019, ApJ, 873, 111
Kollmeier, J. A., Zasowski, G., Rix, H.-W., et al. 2017, arXiv:1711.03234
Lachos, V. H., Labra, F. V., & Ghosh, P. 2014, Pro Mathematica, 28, 11
Lang, D. 2014, AJ, 147, 108
Lawrence, A., Warren, S. J., Almaini, O., et al. 2007, MNRAS, 379, 1599
Luo, A. L., Zhao, Y.-H., Zhao, G., et al. 2015, RAA, 15, 1095
Lyke, B. W., Higley, A. N., McLane, J. N., et al. 2020, ApJS, 250, 8
MacLeod, C. L., Ross, N. P., Lawrence, A., et al. 2016, MNRAS, 457, 389
Martini, P., & Weinberg, D. H. 2001, ApJ, 547, 12
McGreer, I. D., Jiang, L., Fan, X., et al. 2013, ApJ, 768, 105
McMahon, R. G., Banerji, M., Gonzalez, E., et al. 2013, Msngr, 154, 35
Meisner, A. M., Lang, D., Schlafly, E. F., & Schlegel, D. J. 2019, PASP, 131, 124504
Montero-Dorta, A. D., & Prada, F. 2009, MNRAS, 399, 1106
Mortlock, D. J., Warren, S. J., Venemans, B. P., et al. 2011, Natur, 474, 616
Nidever, D. L., Dey, A., Olsen, K., et al. 2018, AJ, 156, 131
Oguri, M., Inada, N., Pindor, B., et al. 2006, AJ, 132, 999
Oguri, M., Inada, N., Strauss, M. A., et al. 2012, AJ, 143, 120
Palanque-Delabrouille, N., Magneville, C., Yèche, C., et al. 2016, A&A, 587, A41
Prochaska, J. X., Hennawi, J. F., Lee, K.-G., et al. 2013, ApJ, 776, 136
Richards, G. T., Weinstein, M. A., Schneider, D. P., et al. 2001, AJ, 122, 1151
Richards, G. T., Strauss, M. A., Fan, X., et al. 2006, AJ, 131, 2766
Robin, A. C., Reylé, C., Derrière, S., & Picaud, S. 2003, A&A, 409, 523
Rumbaugh, N., Shen, Y., Morganson, E., et al. 2018, ApJ, 854, 160
Schlafly, E. F., Meisner, A. M., & Green, G. M. 2019, ApJS, 240, 30
Schlegel, D. J., Finkbeiner, D. P., & Davis, M. 1998, ApJ, 500, 525
Shen, X., Hopkins, P. F., Faucher-Giguère, C.-A., et al. 2020, MNRAS, 495, 3252
Shen, Y., Strauss, M. A., Oguri, M., et al. 2007, AJ, 133, 2222
Shu, Y., Koposov, S. E., Evans, N. W., et al. 2019, MNRAS, 489, 4741
Skrutskie, M. F., Cutri, R. M., Stiening, R., et al. 2006, AJ, 131, 1163
Wang, F., Yang, J., Fan, X., et al. 2021, ApJL, 907, L1
Weinstein, M. A., Richards, G. T., Schneider, D. P., et al. 2004, ApJS, 155, 243
Wolf, C., Hon, W. J., Bian, F., et al. 2020, MNRAS, 491, 1970
Wright, E. L., Eisenhardt, P. R. M., Mainzer, A. K., et al. 2010, AJ, 140, 1868
Wright, E. L., Eisenhardt, P. R. M., Mainzer, A. K., et al. 2019, AllWISE Source Catalog, IPAC, doi:10.26131/IRSA1
Yang, J., Wang, F., Fan, X., et al. 2020, ApJL, 897, L14
Yang, Q., Wu, X.-B., Fan, X., et al. 2017, AJ, 154, 269
Yang, Q., Wu, X.-B., Fan, X., et al. 2018, ApJ, 862, 109
Yao, S., Wu, X.-B., Ai, Y. L., et al. 2019, ApJS, 240, 6
Yèche, C., Petitjean, P., Rich, J., et al. 2010, A&A, 523, A14
York, D. G., Adelman, J., Anderson, J. E., Jr, et al. 2000, AJ, 120, 1579
Yuan, F., Lidman, C., Davis, T. M., et al. 2015, MNRAS, 452, 3047